



1 **Long-term Variability in Black Carbon Emissions Constrained by**
2 **Gap-filled Absorption Aerosol Optical Depth and Associated**
3 **Premature Mortality in China**

4 Wenxin Zhao¹, Yu Zhao^{1,2*}, Yu Zheng³, Dong Chen⁴, Jinyuan Xin⁵, Kaitao Li⁶, Huizheng
5 Che³, Zhengqiang Li⁷, Mingrui Ma¹, Yun Hang⁸

6 1 State Key Laboratory of Pollution Control and Resource Reuse, School of Environment,
7 Nanjing University, 163 Xianlin Rd., Nanjing, Jiangsu 210023, China

8 2 Jiangsu Collaborative Innovation Center of Atmospheric Environment and Equipment
9 Technology (CICAET), Nanjing University of Information Science and Technology,
10 Jiangsu 210044, China

11 3 State Key Laboratory of Severe Weather (LASW) & Key Laboratory of Atmospheric
12 Chemistry of CMA (LAC), Chinese Academy of Meteorological Sciences, Beijing 100081,
13 China

14 4 Jiangsu Provincial Academy of Environmental Science, 176 North Jiangdong Rd., Nanjing,
15 Jiangsu 210036, China

16 5 LAPC, Institute of Atmospheric Physics, Chinese Academy of Sciences, Beijing 100029,
17 China

18 6 School of Information, Space Engineering University, Beijing 101416, China

19 7 State Environmental Protection Key Laboratory of Satellite Remote Sensing, Aerospace
20 Information Research Institute, Chinese Academy of Sciences, Beijing 100101, China

21 8 Gangarosa Department of Environment Health, Rollins School of Public Health, Emory
22 University, 1518 Clifton Road NE, Atlanta, GA 30322, USA

23

24 * Corresponding Author: Yu Zhao

25 Phone: 86-25-89680650; email: yuzhao@nju.edu.cn



26 **Abstract**

27 Black carbon (BC) plays an important role in air quality, public health, and climate,
28 while its long-term variations in emissions and health effect were insufficiently understood
29 for China. Here, we present the spatiotemporal evolution of BC emissions and the associated
30 premature mortality in China during 2000-2020 based on an integrated framework combining
31 satellite observations, a machine learning technique, a “top-down” inversion approach, and an
32 exposure-response model. We found that the “bottom-up” approach likely underestimated BC
33 emissions, particularly in less developed western and remote areas. Pollution controls were
34 estimated to reduce the annual BC emissions by 26% during 2010-2020, reversing the 8%
35 growth during 2000-2010. BC emissions in the main coal-producing provinces declined by
36 2010 but rebounded afterwards. By contrast, provinces with higher economic and
37 urbanization levels experienced emission growth (0.05-0.10 Mg/km²/yr) by 2010 and
38 declined greatly (0.07-0.23 Mg/km²/yr) during 2010-2020. The national annual
39 BC-associated premature mortality ranged between 733,910 (95% confidence interval:
40 676,790-800,250) and 937,980 cases (864,510-1,023,400) for different years. The changing
41 BC emissions contributed 78,590 cases (72,520-85,600) growth within 2000-2005 and
42 133,360 (123,150-145,180) reduction within 2010-2015. Strategies differentiated by region
43 are needed for further reducing BC emissions and its health and climate impacts.



44 **1. Introduction**

45 Black carbon (BC), commonly emitted during incomplete combustion of fossil fuels
46 (Bond et al., 2013; Liu et al., 2022; Shindell et al., 2012), is an important species in airborne
47 fine particulate matter (PM_{2.5}). BC poses greater health risks than total PM_{2.5} due to its
48 absorption and penetration abilities (Li et al., 2016b; Wang et al., 2014; Xue et al., 2021) and
49 is a crucial short-lived climate forcer (Harmsen et al., 2020; Samset et al., 2020). With a large
50 population and high energy consumption, China has become a major contributor of global BC
51 emissions (Lu et al., 2019; Wang et al., 2012) and has suffered from BC-associated climate
52 and health effects since the 2000s (Gu et al., 2020; Liu et al., 2022). Compared to widely
53 measured total PM_{2.5} across the country (Liang et al., 2020; Zhang et al., 2019), fewer BC
54 data are available from ground observations and the spatiotemporal coverage of BC
55 concentrations is far less sufficient (Cui et al., 2015; Tao et al., 2017). As a result, the
56 long-term evolution of BC pollution and its associated health burden remain unclear.

57 Alternatively, satellite observations provide broader spatiotemporal coverage of
58 aerosol-related variables (Schutgens et al., 2021), e.g., aerosol absorption optical depth
59 (AAOD) that reflects light extinction due to light-absorption aerosols including BC. However,
60 most sensors can only monitor total aerosol information rather than individual components
61 (Li et al., 2016a), and cloud cover and surface reflectance cause considerable missing values
62 and uncertainty (Liang et al., 2020; Zhang et al., 2015). For example, the Ozone Monitoring
63 Instrument (OMI) and POLarization and Directionality of the Earth's Reflectance instrument
64 (POLDER) provided long-term national average AAOD coverage of 9%-22% (2005-2020)



65 and 8%-12% (2006-2013) in China, respectively. Satellite-derived AAOD needs to be
66 comprehensively processed to fill gaps in its data and to improve its representativeness of BC
67 before it can be effectively applied.

68 Complete and reliable emission estimates are essential for diagnosing pollution sources
69 and evaluating the benefits of pollution controls. Compared to species generated largely from
70 industrial and energy infrastructures (e.g., SO₂ and NO_x), BC emissions are more challenging
71 to estimate as they are commonly from residential and commercial sources that are more
72 difficult to track (Bond et al., 2013; Li et al., 2017; Zhu et al., 2019). Existing “bottom-up”
73 estimates varied between 0.9 and 2.5 Tg/yr during 2000-2020, with inconsistent interannual
74 changing patterns (European Commission, 2022; Klimont et al., 2009; Kurokawa and Ohara,
75 2020; Lei et al., 2011; Lu et al., 2011; McDuffie et al., 2020; Qin and Xie, 2012; Tsinghua
76 University, 2023; Wang et al., 2014). The uncertainty of those estimates reached up to ±360%
77 due to diverse and quickly changing manufacturing technologies and emission controls
78 (Streets et al., 2003; Wang et al., 2016). Consequently, chemical transport models (CTMs)
79 often underestimate BC concentrations and AAOD, particularly in Asia, ranging from factors
80 of 2-10 (Chen et al., 2019c; Hu et al., 2016; Wang, 2015). To overcome this limitation,
81 “top-down” approaches constraining BC emissions with available observations have been
82 developed and applied to correct BC emissions in China (Cohen and Wang, 2014; Evangeliou
83 et al., 2018; Fu et al., 2012; Guerrette and Henze, 2017; Wang et al., 2013; Zhao et al., 2019).
84 However, restricted by insufficient spatiotemporal coverage, studies were usually conducted
85 for individual years/months and showed considerable discrepancies (Wang et al., 2018;



86 Zhang et al., 2015). Incomplete and inconsistent information could hardly be combined to
87 provide full knowledge of long-term BC emissions. Thus, “bottom-up” emission estimates
88 with great uncertainty were applied in simulating BC exposure and its health burden for
89 limited years (2000, 2013, and 2016, Cui et al., 2022; Qin et al., 2019; Saikawa et al., 2009;
90 Wang et al., 2021). Moreover, few analyses have evaluated the spatiotemporal variations and
91 driving forces of BC-associated health effects. The influence of human activities on quickly
92 changing BC emissions and their associated health impact is inadequately or inaccurately
93 understood, weakening science-based decision making for air pollution control.

94 Herein, we developed an integrated framework combining available satellite
95 observations, an improved machine learning technique, a “top-down” inversion approach,
96 and an exposure-response model to obtain a panoramic perspective of China’s BC emissions
97 and the associated mortality for the past two decades. We first predicted full-coverage
98 monthly AAOD for mainland China during 2000-2020 using an extreme gradient boosting
99 (XGBoost) model. Combining this new dataset with air quality and BC light absorption
100 empirical models, we then improved the “top-down” inversion technique to estimate the
101 interannual changes in BC emissions. We further calculated the BC-associated premature
102 mortality and attributed its interannual changes to individual driving factors. The outcomes
103 highlight an improved BC emission estimation and the influence of human activities on the
104 long-term evolution of BC emissions and the associated health effects, thereby supporting
105 policies coordinating air quality, health, and climate issues.

106



107 **2. Materials and Methods**

108 **2.1 Filling gaps in AAOD data using a machine learning algorithm**

109 We applied the XGBoost model to fill gaps in satellite-derived AAOD data at the
110 monthly level during 2000-2020. XGBoost has been widely used in predicting air pollution
111 and shown to outperform various statistical and machine learning models (Xiao et al., 2018),
112 requiring less training and prediction time than other machine learning techniques such as
113 random forest (see details in Supplementary Text S1). The target domain included mainland
114 China at a horizontal resolution of $0.25^\circ \times 0.25^\circ$ (Supplementary Figure S1).

115 OMI takes advantage of the near-UV algorithm based on the sensitivity of radiances
116 measured at the atmosphere to the varying aerosol species to derive AAOD (Zhang et al.,
117 2017). The algorithm excluded the very small AOD values to reduce the uncertainty of the
118 AAOD retrieval at low AOD values. Previous studies have proven the good agreement
119 between OMI AAOD and AERONET ground observations as well as other satellite
120 observations (Ahn et al., 2008; Zhang et al., 2017). Here we used OMI-derived AAOD at 483
121 nm, obtained from the OMAEROe L3 global aerosol product at a horizontal resolution of
122 $0.25^\circ \times 0.25^\circ$ (Deborah and Pepijn, 2012; <https://disc.gsfc.nasa.gov>; last accessed on 10
123 March 2022), as the dependent variable for model training and validation. For each grid cell,
124 daily AAOD values for no less than 7 days in a given month were averaged as the monthly
125 AAOD value. Owing to its long service time and damage to the satellite sensor, the original
126 spatial coverage of monthly OMI-derived AAOD ranged from 1% to 53%, and was
127 commonly lower for later years than earlier years. The multiyear average coverage was



128 relatively low in southern China (<25%), attributed to cloud cover and high surface
129 reflectance (Supplementary Figure S2).

130 Twenty-four interpretation variables were selected for model training, including aerosol
131 optical, meteorological, geographic, and temporal parameters (Supplementary Table S1).
132 Aerosol optical and meteorological parameters were extracted from the Modern-Era
133 Retrospective analysis for Research and Applications, Version 2 (MERRA-2) dataset at a
134 horizontal resolution of $0.625^\circ \times 0.5^\circ$ (<https://disc.gsfc.nasa.gov>; last accessed on 10 June
135 2022), to reflect the optical properties, transport, and diffusion of pollutants. As ancillary
136 variables associated with BC emission sources and transport conditions, land-use and
137 elevation data were obtained from the Chinese Academy of Sciences at a horizontal
138 resolution of 1×1 km (<https://www.resdc.cn/Default.aspx>; last accessed on 25 June 2022).
139 Bilinear interpolation was applied to interpolate these parameters to a resolution of $0.25^\circ \times$
140 0.25° .

141 For model performance evaluation, we applied a ten-fold Cross-Validation (CV) firstly
142 to evaluate out-of-sample accuracy. The CV process randomly split training data records into
143 10 subsets, in which 9 subsets were used to train models and the remaining one was used to
144 examine the performance. Through ten times repetition of CV, all of the data records were
145 tested once. Besides, we collected monthly AAOD data from four aerosol monitoring
146 networks to further verify the model reliability, including Aerosol Robotic Network
147 (AERONET, <https://aeronet.gsfc.nasa.gov>; last access: 10 March 2022), China Aerosol
148 Remote Sensing Network (CARSNET), Campaign on Atmospheric Aerosol Research



149 Network of China (CARE-China) and Sun Sky Radiometer Observation Network (SONET),
150 as shown in Supplementary Figure S1a. Detailed site descriptions can be found in
151 corresponding studies (Che et al., 2015; Li et al., 2018; Xin et al., 2015). Given the
152 complicated technologies and large costs required for measurement operation, instrument
153 maintenance and calibration, current aerosol monitoring sites are rare and unevenly located in
154 the country. There are clear missing values in time series, and most measurements we
155 collected focused on 2015-2019. All the ground-level AAOD data were interpolated to 483
156 nm using the Angstrom exponent to independently evaluate the performance of machine
157 learning predictions. Model performance was evaluated with selected statistical indicators
158 including correlation coefficient (R), normalized mean error (NME), normalized mean bias
159 (NMB), and root mean squared prediction error (RMSE).

160 **2.2 Constraining BC emissions with gap-filled AAOD and CTM**

161 We developed a “top-down” inversion approach to estimate the monthly BC emissions in
162 China during 2000-2020 (see conceptual diagram in Figure 1). To avoid abundant
163 calculations, five-year intervals were adopted in the simulation, and January, April, July, and
164 October were selected as representative months of different seasons.

165 **2.2.1 Integrated model for AAOD simulation**

166 We simulated AAOD using the Community Multi-scale Air Quality (CMAQ) model
167 version 5.1 and an empirical BC light absorption model. AAOD is defined as the integrated
168 absorption coefficient (m^{-1}) over the atmospheric column, and the absorption coefficient is



169 the product of the mass concentration (g/m^3) and mass absorption efficiency of BC (MAE,
170 m^2/g) (Bond et al., 2013). Prior anthropogenic BC emissions during 2000-2020 were obtained
171 from the Multiresolution Emission Inventory for China (MEIC, <http://www.meicmodel.org>;
172 last accessed on 25 May 2022), and prior BC emissions from open biomass burning were
173 obtained from the Global Fire Emissions Database version 4.1s (GFED V4.1s,
174 <https://www.geo.vu.nl/~gwerf/GFED/GFED4/>; last accessed on 25 May 2022). First, BC
175 concentrations at different vertical layers were simulated using the CMAQ model at a
176 horizontal resolution of 27×27 km (see Supplementary Text S2 for model settings). Based
177 on our previous measurements, we then adopted an empirical model to quantify the enhanced
178 light absorption of the coating on BC particles (Chen et al., 2019b), and obtained the
179 simulated BC AAOD:

$$180 \quad MAE_{i,m,n} = 6.83 - 0.0007 \times \left(\frac{[NA-PM]_{i,m,n}}{[BC]_{i,m,n}} \right)^2 + 0.08 \frac{[NA-PM]_{i,m,n}}{[BC]_{i,m,n}} \quad (1)$$

$$181 \quad AAOD_{sim,i,m,n} = \int_{z0}^z MAE_{i,m,n} \times [BC]_{i,j,m,n} \times dz \quad (2)$$

182 where MAE , $AAOD_{sim}$, and $[BC]$ represent the simulated BC MAE, BC AAOD, and BC
183 concentration, respectively; z and $z0$ represent the simulated top and bottom of the
184 atmosphere (0), respectively; $[NA-PM]$ represents the simulated concentration of total
185 non-absorbing matter (i.e., SO_4^{2-} , NO_3^- , and organic carbon, OC); i and j represent the
186 numbers of grids and vertical layers, respectively; dz represents the height of the vertical
187 layer; and m and n represent the year and month, respectively. (All parameters and variables
188 shown in the equations are summarized in Supplementary Table S2.)



189 2.2.2 Inversion system for BC emissions

190 We developed an inversion system based on the spatiotemporal-dependent relationship
191 between BC emissions and BC AAOD.

192 As AAOD is attributed to all light-absorbing aerosols, including BC, dust, and brown
193 carbon (BrC), we first separated the contribution of BC to the XGBoost-predicted AAOD
194 obtained in Section 2.1, using the fraction of BC in AAOD obtained from MERRA-2:

$$195 \quad AAOD_{BC_xgb_{i,m,n}} = AAOD_{xgb_{i,m,n}} \times \frac{AAOD_{BC_merra2_{i,m,n}}}{AAOD_{merra2_{i,m,n}}} \quad (3)$$

196 where $AAOD_{BC_xgb}$ represents the separated XGBoost BC AAOD; $AAOD_{xgb}$ represents
197 XGBoost AAOD; $AAOD_{BC_merra2}$ represents MERRA-2 BC AAOD; and $AAOD_{merra2}$
198 represents MERRA-2 AAOD. The hourly MERRA-2 data at $0.625^\circ \times 0.5^\circ$ were reallocated
199 to the horizontal resolution of CMAQ model (27 km) and averaged to a monthly level.

200 With XGBoost BC AAOD, we inferred monthly BC emissions with Eq. 4:

$$201 \quad E_{posterior\ i,m,n} = E_{prior\ i,m,n} \times \left(1 + \frac{AAOD_{BC_xgb_{i,m,n}} - AAOD_{sim_{i,m,n}}}{AAOD_{BC_xgb_{i,m,n}}} \times \alpha_{i,m,n}\right) \quad (4)$$

202 where $E_{posterior}$ and E_{prior} represent posterior and prior BC emissions, respectively; $AAOD_{sim}$
203 represents the simulated BC AAOD based on prior BC emissions; and α is a unitless factor
204 representing the sensitivity of changes in BC AAOD to those in BC emissions in each model
205 grid. We carried out a perturbation simulation to obtain α :

$$206 \quad \alpha_{i,m,n} = \frac{\Delta E_{perturbed\ i,m,n}}{E_{prior\ i,m,n}} \div \frac{AAOD_{sim_{perturbed\ i,m,n}} - AAOD_{sim_{prior\ i,m,n}}}{AAOD_{sim_{prior\ i,m,n}}} \quad (5)$$

207 where $prior$ and $perturbed$ represent prior and perturbation simulations, respectively;
208 $\Delta E_{perturbed}/E_{prior}$ represents a 10% reduction in prior BC emissions; and $AAOD_{sim_{perturbed}}$ and



209 $AAOD_{sim_{prior}}$ represent the simulated BC AAOD with the perturbation and prior simulation,
210 respectively.

211 We adopted the posterior BC emissions as the new BC emission input, repeating the
212 simulation until the NME of BC AAOD from CTM and XGBoost was reduced <30%. We
213 evaluated the CMAQ model performance based on our gap-filled AAOD dataset and
214 available observations of surface BC concentrations (Supplementary Table S3). Besides this
215 base case as mentioned above, we conducted four sensitivity tests to recalculate posterior BC
216 emissions, to explore the uncertainty in the inversion (Supplementary Text S3 and Table S4).
217 They respectively applied the estimated AAOD at a longer wavelength of 865 nm (Test 1),
218 the different dust AAOD fractions (Test 2), the adjusted MAE based on observations
219 (Supplementary Table S5; Test 3) and the adjusted simulated BC lifetime (Test 4).

220 **2.3 Estimating the associated mortality burden and determining its drivers**

221 A log-linear model was applied to estimate the attributable fraction (AF) of premature
222 mortality to BC exposure:

$$223 \quad AF(C_{i,m}) = 1 - e^{-\beta_{BC} \times \Delta C_{i,m}} \quad (6)$$

224 where $C_{i,m}$ represents the posterior simulated average BC concentration of four months in
225 year m of grid i , and $\Delta C_{i,m}$ represents the difference between $C_{i,m}$ and the health impact
226 threshold. Due to the lack of reported BC concentration thresholds in current epidemiological
227 studies (Cui et al., 2022), we applied the 1.25th percentile of BC concentrations as the
228 threshold ($0.02 \mu\text{g}/\text{m}^3$). β_{BC} represents the concentration–response coefficient. Here, we used



229 a β_{BC} value of 0.0204 (95% confidence interval (CI): 0.0187-0.0224) based on a unique
230 cohort study conducted in eastern China (Chen et al., 2021).

231 The premature mortality (M) attributable to BC exposure was calculated using Eq. 7:

$$232 \quad M_{i,s,m} = P_{i,m} \times PS_{s,m} \times B_{s,m} \times AF(C_{i,m}) \quad (7)$$

233 where s represents the population subgroup, P represents the population, PS represents the
234 proportion of the population subgroup to the national population, and B represents the
235 national baseline mortality rate of all-cause diseases. The gridded population data were
236 aggregated from the 1 km population density dataset in WorldPop (WorldPop, 2018;
237 <https://hub.worldpop.org/doi/10.5258/SOTON/WP00675>; last accessed on 20 October 2022).

238 We corrected the annual total population using Chinese census data obtained from the State
239 Statistics Bureau (<https://data.stats.gov.cn/>; last accessed on 20 October 2022). The national
240 average population age structure and baseline mortality rate of all-cause diseases were
241 collected from the Global Burden of Disease study (Cohen et al., 2017;
242 <https://vizhub.healthdata.org/gbd-results/>; last accessed on 20 October 2022).

243 We evaluated the impact of each of the four factors in Eq. 7 (three vulnerability factors
244 and BC exposure) on the changing mortality through a series of sensitivity analyses (Cohen et
245 al., 2017; Geng et al., 2021). We established 24 decomposition sequences with the four
246 factors and calculated the mean changing mortality of each factor through all sequences.
247 Moreover, mortality changes attributed to BC exposure were further disaggregated into
248 contributions from BC emissions and meteorological factors using a direct proportion
249 approach with the CMAQ model (Supplementary Text S4).



250 **3. Results and Discussion**

251 **3.1 Gap-filled AAOD during 2000–2020**

252 **3.1.1 Evaluation of XGBoost model performance**

253 By filling the missing values with XGBoost model, we obtain full coverage of monthly
254 AAOD for China from 2000 to 2020. Evaluated by 10-fold CV, the predicted AAOD shows
255 good agreements with OMI observations, with R of 0.92, RMSE of 0.013 and NMB of -4%
256 (Figure 2). Comparison with individual ground measurements further verifies the reliability
257 and robustness of the model across regions and periods, with RMSE of 0.017 and NMB of 5%
258 for all available observations. The comparisons with observations at typical individual sites
259 are shown in Supplementary Figure S5. Overall, better performance is shown by our
260 predictions compared to other AAOD datasets. As a reference, the RMSE and NMB between
261 MERRA-2 and the same observations are 0.021 and -19%, respectively. In addition to
262 evaluation for the whole period, Supplementary Table S8 shows model performance for each
263 year. The performance of 10-fold CV gets moderately poorer for more recent years,
264 accompanied with the reduced sampling size of OMI observations. Regarding the ground
265 observation, better performance appeared in recent years indicated by the smaller RMSE, and
266 the underestimation in earlier years could probably be attributed to less sites available and
267 more difficulty in data quality control.

268 Besides, the spatial coverage of OMI AAOD influences the training data size for
269 XGBoost model and thereby the spatiotemporal pattern of gap-filled AAOD. Supplementary
270 Table S9 shows the XGBoost performance against OMI and ground measurement by OMI



271 coverage. In general, poorer performance was found for areas with more missing values.
272 Evaluated against ground measurement, for example, the RMSE and NMB for areas with
273 OMI coverage less than 20% are 0.019 and 9%, and they decline to 0.015 and 3% for areas
274 with OMI coverage more than 60%. All the biases are kept within limited range. The analysis
275 indicates the satisfying quality of our gap-filled AAOD dataset, with full spatiotemporal
276 coverage for the research domain and period.

277 Supplementary Table S1 summarizes the importance levels of model predictors in the
278 XGBoost model, expressed with three indicators, and “Gain” is the most decisive one.
279 MERRA-2 AAOD, longitude, latitude and temporal parameters are identified as most
280 dominant variables for filling gap of OMI AAOD. Besides, crop coverage is another
281 dominant variable, which reflects the contribution of open biomass burning to light-absorbing
282 aerosol emissions and thereby to AAOD. Specific meteorological parameters (e.g., surface
283 pressure (PS), short-wave radiation flux (SWGDN), evaporation from turbulence (EVAP),
284 and planetary boundary layer height (PBLH)) reflect surface energy budget, transport and
285 diffusion of air pollutants, thus play an important role in AAOD prediction.

286 **3.1.2 Spatiotemporal patterns of XGBoost-predicted AAOD during 2000–2020**

287 Figure 3a illustrates the spatial distribution of the averaged XGBoost-predicted AAOD
288 during 2000-2020. Hot spots mainly existed in eastern China, with a regional average of 0.05,
289 which was higher than the national average of 0.03. The AAOD values of
290 Beijing-Tianjin-Hebei (BTH), Fenwei Plain (FWP), Yangtze River Delta (YRD), Sichuan
291 Basin (SCB), and Northeast China (NE) were 1.4-1.8 times that of the national average, while



292 that of Pearl River Delta (PRD) was much closer to the national average (see Figure S1a for
293 the locations of regions). The relatively small proportion of the rural population to the total
294 population (34%) and highly developed economy in PRD might have resulted in limited
295 light-absorbing aerosol emissions.

296 Figures 3b-h illustrates the interannual variability of the predicted monthly AAOD for
297 China and the key regions during 2000-2020, which were divided into two temporal phases.
298 In phase 1 (2000-2012), the AAOD of China experienced a slight decline ($-6.94 \times 10^{-5}/\text{yr}$)
299 while those of key regions moderately increased, except FWP. The annual AAOD growth of
300 the most economically developed regions (BTH, YRD, and PRD) ranged 1.13×10^{-4} - 5.20×10^{-4}
301 /yr, larger than those in other regions (SCB and NE, 2.84×10^{-7} - 7.54×10^{-5} /yr), reflecting the
302 influence of regional differences based on human activities and meteorological conditions.
303 Increasing industrial production and residential combustion elevated anthropogenic emissions
304 of light-absorbing aerosols, thereby increasing AAOD values in key regions. However,
305 nationwide increasing precipitation during phase 1 ($0.3 \text{ g/m}^2/\text{s}/\text{yr}$ indicated by MERRA-2)
306 may have enhanced the removal of pollutants and offset the effects of increasing emissions.
307 In addition, strengthened afforestation policies in northern China led to a decline in dust
308 aerosol emissions and thus the AAOD values during this period (Middleton, 2019).

309 In phase 2 (2013-2020), the AAOD of China demonstrated a clear decline ($1.99 \times$
310 $10^{-4}/\text{yr}$), with faster rates in key regions (3.61×10^{-4} - $1.42 \times 10^{-3}/\text{yr}$). The AAOD decline in
311 key regions in phase 2 was much faster than its growth in phase 1, indicating the benefits of
312 China's air pollution controls, such as implementation of the strictest ever emission standards



313 in the industrial sector and promotion of clean energy use for household heating and cooking.
314 AAOD growth clearly occurred in northern regions from 2018 onwards ($2.60\text{-}3.56 \times 10^{-3}/\text{yr}$),
315 which differed from its continuous decrease in southern regions. The increasing surface wind
316 speed in northern regions elevated the frequency of sandstorms, resulting in greater regional
317 emissions of light-absorbing dust aerosols that partly contributed to AAOD growth (Yang et
318 al., 2021).

319 **3.2 Long-term evolution of constrained BC emissions during 2000–2020**

320 **3.2.1 Verification of constrained BC emissions**

321 We find that application of posterior BC emissions constrained by XGBoost-predicted
322 AAOD (described in detail in Section 3.2.2) largely improved the model performance of BC
323 concentration and AAOD simulation compared with use of prior BC emissions.

324 With acceptable performance of meteorological simulation (Supplementary Table S10),
325 the CMAQ model presented a clear underestimation of surface BC concentrations based on
326 the prior BC emissions, with the NMB and NME calculated to be -46% and 53% ,
327 respectively (Figure 4). Besides, larger underestimation appeared for the very early and most
328 recent year, with NMB calculated at -59% and -60% for 2000 and 2020, respectively
329 (Supplementary Figure S6). Application of posterior BC emissions greatly reduced the NMB
330 and NME within the research period to -14% and 36% , respectively (Figure 4). As a
331 reference, the performance meets the benchmark of BC simulation (NMB $< \pm 20\%$ and NME
332 $< 45\%$) proposed by Huang et al. (2021). Moreover, improved model performance has been
333 achieved for all the years with largely reduced NMB and NME compared to simulations with



334 the prior emissions (Supplementary Figure S6). Larger uncertainty for 2000 may be caused
335 by limited observation and less-controlled data quality for earlier years.

336 We also compare the simulated and observed BC concentrations by land use type
337 (Supplementary Figure S7). Application of the prior emissions resulted in more
338 underestimation of BC concentration for the forest and grassland regions (NMB: -51%~-77%;
339 NME: 51%~77%) compared to urban and rural regions (NMB: -35%~-51%; NME:
340 47%~51%). The model performance was clearly improved for all the land use types when the
341 posterior emissions were applied. In particular the NMB and NME were calculated to
342 respectively range -2%~-40% and 31%~52%, for the forest and grassland regions. The
343 evaluation supported our estimates of posterior emissions, not only for areas with insensitive
344 human activities (e.g., urban regions) but also remote regions.

345 Similarly, Simulation of AAOD based on the prior emissions presented a clear
346 underestimation compared with the OMI-derived observations, with the monthly NMB and
347 NME ranging -85%~-29% and 34%~85%, respectively (Supplementary Table S11). As
348 pointed by Bond et al. (2013), the incorrect assumption of mixing state of BC in the CTM
349 could result in the general underestimation of MAE, and thereby AAOD. Clear improvement
350 in the performance of AAOD simulation can be found when the posterior emissions were
351 applied. The NMB, NME, and RMSE were calculated to range -11%~14%, 15%~28%, and
352 0.01~0.03, respectively, much smaller than those with the prior emissions, while R was
353 largely elevated from 0.15~0.86 to 0.73~0.95.



354 **3.2.2 Spatiotemporal patterns of posterior BC emissions and differences between prior**
355 **and posterior BC emissions**

356 Figures 5a–c presents the spatial distribution of multiyear averages of the prior and
357 posterior BC emissions and their relative differences (see details for individual years in
358 Figure 6). The annual total posterior BC emissions were estimated to increase from 6.48 Tg
359 in 2000 to 7.03 Tg in 2010 and decrease to 5.21 Tg in 2020. Compared with the prior BC
360 emissions, the posterior BC emissions presented a clear enhancement, with a multiyear
361 average factor of 3.3 for the entire country (Figure 5c). The value declined from 3.7 to 2.7
362 during 2000–2015, but rose again to 4.1 in 2020 (Figure 5d). The posterior BC emissions also
363 presented an enhancement compared to other “bottom–up” estimates of China’s BC
364 emissions, with the lowest factor of 1.7 for the Peking University Fuel Inventory (PKU-Fuel,
365 <http://inventory.pku.edu.cn/>; last accessed on 1 May 2023) and highest factor of 4.3 for the
366 Emissions Database for Global Atmospheric Research (EDGAR,
367 https://edgar.jrc.ec.europa.eu/dataset_ap61; last accessed on 1 May 2023) (Figure 5d and
368 Table 1). The comparisons between “bottom–up” and “top–down” estimates of BC emissions
369 suggested a possible underestimation of the former, resulting partly from the under-reporting
370 of activity levels and lack of local measurements for specific BC emission factors (EFs,
371 emissions per unit of activity level) (Fu et al., 2012; Guan et al., 2012). In addition, the
372 omission of small fires from satellite observations and application of global EFs led to an
373 underestimation of biomass burning emissions (Yang and Zhao, 2019). Along with improved
374 energy and economic statistics and the increased amount of EF data obtained through field
375 observations, the discrepancy between prior and posterior BC emissions was gradually



376 reduced until 2020. The increased uncertainty in prior BC emissions in 2020 may have
377 resulted partly from an underestimation of increased fuel use owing to residential heating and
378 cooking during the COVID-19 lockdown and quarantine (Zheng et al., 2020).

379 The posterior emissions presented a smaller interannual variability compared to the prior
380 and other “bottom-up” estimates, with a net growth of 8% during 2000-2010 (the analogous
381 numbers are 13%-57% for various “bottom-up” estimates including 24% for the prior used in
382 this work, MEIC+GFED) and a decline of 26% during 2010-2020 (41% for MEIC+GFED,
383 Figure 5e). Besides residential sources, prior emission estimate bias may also have occurred
384 in the transportation sector, such as extra emissions derived from inadequately eliminated
385 vehicles with relatively old standards and the use of specific after-treatment technologies (e.g.,
386 diesel particulate filters) causing the release of ultrafine particles (Louis et al., 2016).

387 Relatively smaller differences between posterior and prior BC emissions were found in
388 eastern China, with a multiyear average of posterior to prior BC emission ratio estimated at
389 2.4, while that for the rest of China reached 8.0 (Figure 5f). The relative differences between
390 posterior and other “bottom-up” BC emission estimates were smaller (1.1-2.1) in more
391 economically developed regions (BTH, FWP, YRD, and PRD), but larger (3.6-6.0) in SCB,
392 NE, and other regions (Table 1). To further explore the impact of human activities on BC
393 emissions, we divided the country into different land use types (Supplementary Figure S1b).
394 The multiyear average BC emission intensity in urban areas was estimated at 1.86 Mg/km²/yr,
395 higher than 1.47 Mg/km²/yr in rural areas (Table 2). Industrial production, transportation, and
396 commercial activities generate abundant emissions in urban areas, while straw burning,



397 residential cooking, and heating are important emission sources in rural areas. Smaller BC
398 emission intensity was estimated in regions less influenced by human activities, i.e., 0.84,
399 0.33, and 0.11 Mg/km²/yr for forest, grassland, and unused regions, respectively. As shown in
400 Figure 5f, the relative differences between posterior and prior BC emissions were smallest in
401 urban areas, with a multiyear average enhancement factor of 1.6, followed by rural areas
402 (factor of 2.6), forest (factor of 4.3), and grassland (factor of 5.5). In general, the “bottom-up”
403 approach could capture information about energy consumption and pollution controls more
404 easily and accurately in regions with more intensive human activities. Such advantages
405 helped reduce the uncertainty in emission estimates for developed urban areas compared with
406 that in remote areas. However, current official statistics do not sufficiently report biofuel
407 consumption and are believed to greatly underestimate raw coal consumption in rural areas
408 (Zhi et al., 2017; Zhu et al., 2019). Limited small fire detection ability via satellite also led to
409 an underestimation of open biomass burning in forest and grassland areas (Schroeder et al.,
410 2008; Yang and Zhao, 2019). Such limitations resulted in a greater underestimation of prior
411 BC emissions in rural and remote regions compared to urban regions (Figure S7).

412 Previous limited studies employing “top-down” approaches estimated China’s BC
413 emissions at 5.7, 3.1, and 2.5 Tg/yr for 2000, 2006, and 2008 (Cohen and Wang, 2014; Fu et
414 al., 2012; Wang et al., 2016), respectively. These studies presented an 0.6-5 times
415 enhancement of posterior BC emissions compared to prior BC emissions (Chen et al., 2019a;
416 Cohen and Wang, 2014; Fu et al., 2012; Wang et al., 2016; Zhang et al., 2015), showing a
417 wider range than the results presented in the current study (2.7-4.1). This discrepancy may



418 have resulted from the application of different inversion approaches, observational data, and
419 prior BC emissions. Moreover, the posterior BC emissions applied in previous studies were
420 lower than those used in the current study for corresponding years by a factor of 12%–64%.
421 In general, incomplete spatial coverage in previous studies limited the emission inversion
422 capability in regions far away from observational sites.

423 **3.2.3 Influence of social and economic development on BC emissions**

424 To explore the influence of social and economic development on BC emissions, we
425 analyzed the diverse changing patterns in posterior BC emission intensity (Mg/km^2) by
426 province, based on rural population fraction, provincial proportion of coal production to the
427 national total, and industrial gross domestic product (GDP).

428 Shanxi, Inner Mongolia, Henan, and Shaanxi were identified as the main coal-producing
429 provinces, collectively contributing 50% and 68% to national total coal production in China
430 during 2000-2010 and 2010-2020, respectively. Shanxi, Henan, and Shaanxi experienced a
431 decline in posterior BC emission intensity during 2000-2010, with annual average decreasing
432 rates estimated at 0.13, 0.03, and 0.02 $\text{Mg}/\text{km}^2/\text{yr}$, respectively (Figure 7a). These provinces
433 have long suffered air pollution from coal burning and the coal industry's structure and
434 technology were improved earlier than in other provinces. For example, Shanxi eliminated
435 over 7000 small coal mines and an outdated production capacity of 385 million tons of coal
436 during 2000-2010 (The Central People's Government of the People's Republic of China, 2011;
437 Han and Wang, 2015). These measures significantly improved coal consumption efficiency,
438 resulting in a sharp decline in BC emission intensity.



439 In comparison, slower decline or even growth in BC emission intensity was
440 demonstrated in Shanxi and Henan during 2010-2020, with changing rates of -0.007 and
441 $0.004 \text{ Mg/km}^2/\text{yr}$, respectively (Figure 7b). Merging and reorganization of the coal industry
442 in these two provinces enhanced coal production and consumption in recent years, thereby
443 reducing the benefits of BC emission controls. Comparatively faster declines were
444 demonstrated in Inner Mongolia and Shaanxi, with decreasing rates of 0.01 and 0.03
445 $\text{Mg/km}^2/\text{yr}$, respectively (Figure 7b). The proportion of coal production in Inner Mongolia
446 and Shaanxi increased from 8% and 2% in 2000 to 28% and 17% in 2020, respectively,
447 demonstrating the increasingly important role of national coal production in these two
448 provinces (Figures 7c and d). Compared with Shanxi and Henan, relatively later but greater
449 efforts were made to improve the coal industry's structure in Inner Mongolia and Shaanxi,
450 leading to considerable BC emission reductions after 2010.

451 Increasing emission intensities were found for most other provinces during 2000-2010,
452 particularly those with high industrial GDP (larger circles in Figure 7c). Prominent BC
453 emission intensity growth was demonstrated in Jiangsu, Shandong, and Beijing, with the
454 annual average growth rates ranging from 0.05 to $0.10 \text{ Mg/km}^2/\text{yr}$. Intensive industrial
455 production activities in these provinces/cities resulted in quickly increasing emissions.
456 Second to industry-developed regions, Anhui, Guangxi, and Yunnan experienced BC
457 emission growth rates of 0.03 - $0.05 \text{ Mg/km}^2/\text{yr}$. In these provinces with higher rural
458 population fractions, the enhanced consumption of household solid fuel and limited progress



459 in air pollution controls led to fast BC emission growth, along with increased demand for
460 living standard improvements.

461 During 2010-2020, BC emission intensities were estimated to decline for most provinces
462 (Figure 7b), and faster decline commonly occurred in provinces with higher urbanization and
463 industrial GDP levels (darker blue and larger circles from right to left on the x-axis in Figure
464 7d). The greatest reductions were demonstrated in Shanghai, Liaoning, Chongqing, Jiangsu,
465 and Fujian, with the decreasing rate ranging from 0.07 to 0.23 Mg/km²/yr. Within this period,
466 stringent pollution controls in the industrial and transportation sectors took effect, particularly
467 in economically developed and highly urbanized regions, resulting in a faster decline in BC
468 emissions compared with less developed regions. Meanwhile, reduced rural population
469 proportion and increased clean energy use jointly restrained household BC emissions.

470 **3.2.4 Comparison of emission and concentration trends for multiple species**

471 We compare the interannual changes in posterior BC emissions with those in national
472 PM_{2.5}, OC, and BC emissions (i.e., prior BC emissions) derived from MEIC, PM_{2.5}
473 concentrations derived from Tracking Air Pollution in China (<http://tapdata.org.cn/>; last
474 accessed on 31 January 2023), and CMAQ-simulated BC concentrations based on posterior
475 BC emissions (Figure 8). During 2005-2020, the annual BC emissions were estimated to
476 decline by 26% (posterior BC emissions) or 43% (prior BC emissions), which was slower
477 than PM_{2.5} (56%), and the relative reduction in BC concentration (14%) was less than that in
478 PM_{2.5} (35%). Compared to total PM_{2.5}, for which the health effects are widely recognized,
479 more attention should be paid to the health effects and control of BC emissions, given its



480 relatively slower decline in ambient concentrations and well-acknowledged higher health
481 risks (Wang et al., 2021; see our estimate on the mortality attributable to BC exposure in
482 Section 3.3). Moreover, the comparison between emission trends in warming (BC) and
483 cooling (e.g., OC) species reveals a climate challenge. Faster decline in OC emissions (47%
484 during 2005-2020) was estimated than in BC emissions, resulting mainly from greatly
485 reduced biofuel use and biomass burning. In contrast, development of the transportation and
486 industrial sectors makes further reductions in BC emissions challenging, and more effective
487 strategy on BC emission controls are urgently needed to restrain climate warming in the
488 future.

489 **3.3 Mortality attributable to BC exposure and its drivers**

490 The all-cause premature deaths attributed to BC increased from 733,910 cases (95% CI:
491 676,790-800,250) in 2000 to 903,030 cases (832,830-984,530) in 2005, decreased to 857,510
492 cases (790,500-935,370) in 2015, and finally reached the highest level at 937,980 cases
493 (864,510-1,023,400) in 2020 (Figure 9). With different BC exposure levels and β_{BC} used, for
494 comparison, more diverse results were presented by previous studies ranging
495 265,120-1,436,960 cases (Cui et al., 2022; Qin et al., 2019; Saikawa et al., 2009; Wang et al.,
496 2021). More premature deaths in eastern China (Supplementary Figure S8) were attributed
497 mainly to the relatively high population density and BC exposure from developed industrial
498 and commercial activities. The highest multiyear average of premature mortality per grid cell
499 was 1080 cases/grid in Shanghai, followed by 578, 555, 379, 328, and 322 cases/grid in



500 Beijing, Tianjin, Jiangsu, Henan, and Shandong, respectively (Table 3). These values were
501 much higher than the national average of 63 cases/grid.

502 Also shown in Figure 9 are the contributions of major factors to the national changing
503 mortality during 2000-2020 (provincial-level results are presented in Table S12). The
504 changing emission levels played an important role in premature mortality. Along with swift
505 growth in the economy and energy consumption from 2000 to 2010, increasing BC emissions
506 enhanced health risks in China and most provinces. The largest increase in national annual
507 mortality was demonstrated during 2000-2005 (78,590 cases, 95% CI: 72,520-85,600).
508 However, BC emission reductions in the main coal-producing provinces, i.e., Shanxi, Henan,
509 and Sichuan, reduced regional health risks during 2005-2010, with declines in annual
510 mortality of 14,320, 13,580, and 8,410 cases, respectively. Benefiting from improved air
511 pollution controls from 2010 to 2020, declining health risks associated with BC emission
512 reduction were demonstrated in China and most provinces. The largest decline in national
513 annual mortality associated with BC emission reduction was demonstrated during 2010-2015
514 (133,360 cases, 123,150-145,180). BC emission rebound in Shanxi and Henan elevated
515 regional health risks during 2015-2020, with increases in annual mortality of 7,170 and 6,190
516 cases, respectively.

517 Varying meteorological conditions also affected the health burden. With the exception
518 of 2005-2010, meteorological conditions were estimated to increase BC exposure and the
519 associated mortality for most of the research period, particularly in eastern China
520 (Supplementary Figure S9). Among vulnerability factors, population aging contributed most



521 to the increased BC-related health burden, elevating the annual national mortality by
522 99,800-142,310 cases for the various five-year intervals. Population growth contributed
523 modestly to the increased health burden in most provinces, with annual national total changes
524 of 10,940-21,230 cases. Exceptions included Sichuan and Hubei, where reduced populations
525 resulted in declining mature mortality. Improved healthcare partly offset the adverse effect,
526 with the annual avoided deaths increasing from 70,100 cases during 2000-2005 to 120,440
527 cases during 2010-2015. This positive effect shrank to 56,690 cases during 2015-2020. With
528 increased population aging and reduced potential of medical care improvement, greater BC
529 emission abatement will be needed to further prevent the health damage.

530 **3.4 Uncertainty analysis**

531 The uncertainties in our results are mainly attributed to separating the contribution of BC
532 to AAOD, simulating BC AAOD based on WRF-CMAQ and the empirical light absorption
533 model, and estimating the premature mortality attributable to BC. Due to the limited number
534 of studies reporting spatiotemporal variability in BrC and dust light absorption in China, we
535 separated BC AAOD based on the MERRA-2 dataset, which may underestimate BrC light
536 absorption at 483 nm (Buchard et al., 2017). Herein, the multiyear average BrC share in
537 AAOD was estimated at 16% (MERRA-2) in eastern China (Supplementary Figure S10),
538 lower than that based on observations (18%–44%, Chen et al., 2019d; Li et al., 2019; Zhu et
539 al., 2021). Notably, the multiyear average of posterior BC emissions using AAOD at a longer
540 wavelength (865 nm) with little BrC effect was estimated to be 11% lower than that using
541 483 nm (Test 1 in Supplementary Text S3 and Figure 10). The posterior BC emissions based



542 on the dust light absorption fraction to AAOD from Copernicus Atmosphere Monitoring
543 Service (CAMS), which was only half that of MERRA-2 (Figure S3), were estimated to be
544 very close to those of Test 1 (Test 2 in Text S3 and Figure 10). In addition, we adopted an
545 empirical model based on observations from one city to simulate MAE. Even with improved
546 performance compared to the average level of multiple CTMs at the global scale (Gliß et al.,
547 2021), our model underestimated MAE and presented smaller regional heterogeneity than
548 existing observations, likely due to the limited spatial extrapolation ability. When MAE was
549 modified according to available observations across the country, the multiyear average of
550 posterior BC emissions was estimated to be 10% lower than that without MAE modification
551 (Test 3 in Text S3 and Figure 10). Besides, the removal processes in CMAQ also affect the
552 BC lifetime simulation and thereby its atmospheric column concentration and emission
553 inversion. The simulated lifetime of 4.7 days in the base case is within the range of 3.8~11.4
554 days reported by previous studies (Figure S4, Bond et al., 2013; Vignati et al., 2010). By
555 adjusting the simulated BC lifetime to the multi-model average level (5.5 days, Gliß et al.,
556 2021), the posterior emissions were estimated 4% smaller compared to those of the base case
557 (Text S3 and Figure 10). Although modest uncertainties were revealed by the above
558 sensitivity tests, they did not change the main findings of this study, with similar interannual
559 variabilities between the base and sensitivity test cases (Figure 10). These uncertainties
560 should be reduced with improved spatiotemporal coverage of BC, BrC and dust
561 light-absorption observations.



562 Furthermore, the health impact estimation could be biased by rare domestic β_{BC} values in
563 China. Previous studies commonly adopted the same functions as $PM_{2.5}$ (Saikawa et al., 2009)
564 or β_{BC} values obtained from American or European studies (Wang et al., 2021), resulting in
565 large uncertainty. Herein, we relied on a unique cohort study in China and calculated the
566 all-cause premature deaths attributed to BC at 733,910-937,980/yr. The β_{BC} values obtained
567 from national-scale studies in the US and Europe indicate a 10-fold difference
568 (220,980-2,386,060/yr, Supplementary Table S13), similar to the estimation conducted in the
569 US (Li et al., 2016b). More domestic epidemiological studies focusing on BC emissions are
570 expected to further reduce the uncertainty.

571 **4. Concluding remarks**

572 Compared to previous studies with nonconsecutive or incomparable estimates, this study
573 provides a panoramic view of the spatiotemporal patterns of AAOD, BC emissions, and the
574 associated mortality in China for the past two decades. We found that the “bottom-up”
575 approach likely underestimated BC emissions, particularly in less developed western and
576 remote areas. Our findings also reveal the influence of human activities on the evolution of
577 BC emissions and the remarkable emission abatement resulting from the implementation of
578 national pollution controls, particularly in developed regions. Pollution controls were
579 estimated to reduce the annual BC emissions by 26% during 2010-2020, reversing the 8%
580 growth during 2000-2010. However, the benefits were smaller than those previously
581 estimated employing the “bottom-up” approach, which likely overestimated progress in



582 pollution controls for certain sources, like the transportation sector and residential solid fuel
583 burning. The long-term BC emission trends in this study address both health and climate risks
584 combined with the effects of other short-lived aerosol species.

585 The energy transition path to achieve China's goal of peak emissions and carbon
586 neutrality provides an opportunity to further reduce BC emissions. Compared to developed
587 regions, the energy transition and emission abatement is more challenging in coal-producing
588 and less-urbanized regions, thus region-specific emission controls should be formulated. For
589 the main coal-producing provinces, BC emissions have declined much slower than those in
590 economically developed provinces or even rebounded along with increased industrial
591 production capacity and energy demand in recent years. As China's traditional energy base,
592 these provinces need to accelerate energy infrastructure adjustments and reduce their
593 dependence on coal, through, for example, the development of photovoltaic and wind power.
594 In addition, aggressively promoting advanced manufacturing technology is recommended.
595 For example, expanding the coal-chemical industry chain could shift the role of coal
596 consumption from traditional fuel to raw material, thus achieving its clean utilization (e.g.,
597 coal liquefaction and gasification technique). For less-urbanized regions, solid fuel, including
598 coal, firewood, and crop residues, remain major energy sources, and actual BC emissions in
599 rural areas could be greatly underestimated compared to those in urban areas. Expansion of
600 natural gas and electricity use for cooking and heating could effectively limit BC emissions in
601 these regions. These efforts can be supported through better infrastructure development and
602 subsidy policy design in the future.



603 **Data availability**

604 The gap-filled AAOD and posterior BC emissions will be available at
605 <http://www.airqualitynju.com/En/Data/List/Datadownload> once the paper is published.

606 **Author contributions**

607 WZhao developed the methodology, conducted the research, performed the analyses and
608 wrote the draft. YZhao developed the strategy, designed the research and revised the
609 manuscript. DChen and MMa provided the support of air quality modeling. HChe, YZhen,
610 JXin, ZLi, KLi and YHang provided the support of AAOD data.

611 **Competing interests**

612 The authors declare that they have no conflict of interest.

613 **Acknowledgements**

614 This work was sponsored by the Natural Science Foundation of China (42177080) and
615 the Key Research and Development Programme of Jiangsu Province (BE2022838). We thank
616 Qiang Zhang from Tsinghua University for the emission data (MEIC) and Cheng Huang from
617 Shanghai Academy of Environmental Sciences (SAES) for BC observation data. We also
618 appreciate Jiandong Wang from Nanjing University of Information Science Information
619 Science and Technology for advices on BC lifetime analysis.



620 **REFERENCES**

- 621 Ahn, C., Torres, O., and Bhartia, P. K.: Comparison of Ozone Monitoring Instrument UV
622 Aerosol Products with Aqua/Moderate Resolution Imaging Spectroradiometer and
623 Multiangle Imaging Spectroradiometer observations in 2006, *J. Geophys. Res.-Atmos.*,
624 113, <https://doi.org/10.1029/2007jd008832>, 2008.
- 625 Bond, T. C., Doherty, S. J., Fahey, D. W., Forster, P. M., Berntsen, T., DeAngelo, B. J.,
626 Flanner, M. G., Ghan, S., Karcher, B., Koch, D., Kinne, S., Kondo, Y., Quinn, P. K.,
627 Sarofim, M. C., Schultz, M. G., Schulz, M., Venkataraman, C., Zhang, H., Zhang, S.,
628 Bellouin, N., Guttikunda, S. K., Hopke, P. K., Jacobson, M. Z., Kaiser, J. W., Klimont,
629 Z., Lohmann, U., Schwarz, J. P., Shindell, D., Storelvmo, T., Warren, S. G., and Zender,
630 C. S.: Bounding the role of black carbon in the climate system: A scientific assessment,
631 *J. Geophys. Res.-Atmos.*, 118, 5380-5552, <https://doi.org/10.1002/jgrd.50171>, 2013.
- 632 Buchard, V., Randles, C. A., da Silva, A. M., Darmenov, A., Colarco, P. R., Govindaraju, R.,
633 Ferrare, R., Hair, J., Beyersdorf, A. J., Ziemba, L. D., and Yu, H.: The MERRA-2
634 Aerosol Reanalysis, 1980 Onward. Part II: Evaluation and Case Studies, *J. Clim.*, 30,
635 6851-6872, <https://doi.org/10.1175/jcli-d-16-0613.1>, 2017.
- 636 Che, H., Zhang, X. Y., Xia, X., Goloub, P., Holben, B., Zhao, H., Wang, Y., Zhang, X. C.,
637 Wang, H., Blarel, L., Damiri, B., Zhang, R., Deng, X., Ma, Y., Wang, T., Geng, F., Qi,
638 B., Zhu, J., Yu, J., Chen, Q., and Shi, G.: Ground-based aerosol climatology of China:
639 aerosol optical depths from the China Aerosol Remote Sensing Network (CARSNET)
640 2002-2013, *Atmos. Chem. Phys.*, 15, 7619-7652,
641 <https://doi.org/10.5194/acp-15-7619-2015>, 2015.
- 642 Chen, C., Dubovik, O., Henze, D. K., Chin, M., Lapyonok, T., Schuster, G. L., Ducos, F.,
643 Fuertes, D., Litvinov, P., Li, L., Lopatin, A., Hu, Q. Y., and Torres, B.: Constraining
644 global aerosol emissions using POLDER/PARASOL satellite remote sensing
645 observations, *Atmos. Chem. Phys.*, 19, 14585-14606,
646 <https://doi.org/10.5194/acp-19-14585-2019>, 2019a.



- 647 Chen, D., Zhao, Y., Lyu, R. T., Wu, R. R., Dai, L., Zhao, Y., Chen, F., Zhang, J., Yu, H., and
648 Guan, M.: Seasonal and spatial variations of optical properties of light absorbing carbon
649 and its influencing factors in a typical polluted city in Yangtze River Delta, China,
650 *Atmos. Environ.*, 199, 45-54, <https://doi.org/10.1016/j.atmosenv.2018.11.022>, 2019b.
- 651 Chen, L., Gao, Y., Zhang, M. G., Fu, J. S., Zhu, J., Liao, H., Li, J. L., Huang, K., Ge, B. Z.,
652 Wang, X. M., Lam, Y. F., Lin, C. Y., Itahashi, S., Nagashima, T., Kajino, M., Yamaji,
653 K., Wang, Z. F., and Kurokawa, J.: MICS-Asia III: multi-model comparison and
654 evaluation of aerosol over East Asia, *Atmos. Chem. Phys.*, 19, 11911-11937,
655 <https://doi.org/10.5194/acp-19-11911-2019>, 2019c.
- 656 Chen, S., Russell, L. M., Cappa, C. D., Zhang, X., Kleeman, M. J., Kumar, A., Liu, D., and
657 Ramanathan, V.: Comparing black and brown carbon absorption from AERONET and
658 surface measurements at wintertime Fresno, *Atmos. Environ.*, 199, 164-176,
659 <https://doi.org/https://doi.org/10.1016/j.atmosenv.2018.11.032>, 2019d.
- 660 Chen, Y., Chen, R., Chen, Y., Dong, X., Zhu, J., Liu, C., van Donkelaar, A., Martin, R. V., Li,
661 H., Kan, H., Jiang, Q., and Fu, C.: The prospective effects of long-term exposure to
662 ambient PM_{2.5} and constituents on mortality in rural East China, *Chemosphere*, 280,
663 130740, <https://doi.org/10.1016/j.chemosphere.2021.130740>, 2021.
- 664 Cohen, A. J., Brauer, M., Burnett, R., Anderson, H. R., Frostad, J., Estep, K., Balakrishnan,
665 K., Brunekreef, B., Dandona, L., Dandona, R., Feigin, V., Freedman, G., Hubbell, B.,
666 Jobling, A., Kan, H., Knibbs, L., Liu, Y., Martin, R., Morawska, L., Pope, C. A., Shin,
667 H., Straif, K., Shaddick, G., Thomas, M., van Dingenen, R., van Donkelaar, A., Vos, T.,
668 Murray, C. J. L., and Forouzanfar, M. H.: Estimates and 25-year trends of the global
669 burden of disease attributable to ambient air pollution: an analysis of data from the
670 Global Burden of Diseases Study 2015, *The Lancet*, 389, 1907-1918,
671 [https://doi.org/10.1016/s0140-6736\(17\)30505-6](https://doi.org/10.1016/s0140-6736(17)30505-6), 2017.
- 672 Cohen, J. B. and Wang, C.: Estimating global black carbon emissions using a top-down
673 Kalman Filter approach, *J. Geophys. Res.-Atmos.*, 119, 307-323,
674 <https://doi.org/10.1002/2013jd019912>, 2014.



- 675 Cui, C., Liu, Y., Chen, L., Liang, S., Shan, M., Zhao, J., Liu, Y., Yu, S., Sun, Y., Mao, J.,
676 Zhang, H., Gao, S., and Ma, Z.: Assessing public health and economic loss associated
677 with black carbon exposure using monitoring and MERRA-2 data, *Environ. Pollut.*, 313,
678 120190, <https://doi.org/10.1016/j.envpol.2022.120190>, 2022.
- 679 Cui, H., Mao, P., Zhao, Y., Nielsen, C. P., and Zhang, J.: Patterns in atmospheric
680 carbonaceous aerosols in China: emission estimates and observed concentrations, *Atmos.*
681 *Chem. Phys.*, 15, 8657-8678, <https://doi.org/10.5194/acp-15-8657-2015>, 2015.
- 682 Deborah, S. Z. and Pepijn, V.: OMI/Aura Multi-wavelength Aerosol Optical Depth and
683 Single Scattering Albedo L3 1 day Best Pixel in 0.25 degree x 0.25 degree V3. NASA
684 Goddard Space Flight Center, Goddard Earth Sciences Data and Information Services
685 Center (GES DISC). Accessed: [10 March 2022], 10.5067/Aura/OMI/DATA3004,
686 2012.
- 687 European Commission, Joint Research Center (EC-JRC)/Netherlands Environmental
688 Assessment Agency (PBL): Emissions Database for Global Atmospheric Research
689 (EDGAR), release EDGAR v6.1_AP (1970 - 2018) of May 2022 [dataset], Accessed:
690 [10 May 2023]. https://edgar.jrc.ec.europa.eu/dataset_ap61, 2022.
- 691 Evangeliou, N., Thompson, R. L., Eckhardt, S., and Stohl, A.: Top-down estimates of black
692 carbon emissions at high latitudes using an atmospheric transport model and a Bayesian
693 inversion framework, *Atmos. Chem. Phys.*, 18, 15307-15327,
694 <https://doi.org/10.5194/acp-18-15307-2018>, 2018.
- 695 Fu, T. M., Cao, J. J., Zhang, X. Y., Lee, S. C., Zhang, Q., Han, Y. M., Qu, W. J., Han, Z.,
696 Zhang, R., Wang, Y. X., Chen, D., and Henze, D. K.: Carbonaceous aerosols in China:
697 top-down constraints on primary sources and estimation of secondary contribution,
698 *Atmos. Chem. Phys.*, 12, 2725-2746, <https://doi.org/10.5194/acp-12-2725-2012>, 2012.
- 699 Geng, G., Zheng, Y., Zhang, Q., Xue, T., Zhao, H., Tong, D., Zheng, B., Li, M., Liu, F.,
700 Hong, C., He, K., and Davis, S. J.: Drivers of PM_{2.5} air pollution deaths in China 2002–
701 2017, *Nat. Geosci.*, 14, 645–650, <https://doi.org/10.1038/s41561-021-00792-3>, 2021.



- 702 Gliß, J., Mortier, A., Schulz, M., Andrews, E., Balkanski, Y., Bauer, S. E., Benedictow, A. M.
703 K., Bian, H., Checa-Garcia, R., Chin, M., Ginoux, P., Griesfeller, J. J., Heckel, A.,
704 Kipling, Z., Kirkevåg, A., Kokkola, H., Laj, P., Le Sager, P., Lund, M. T., Lund Myhre,
705 C., Matsui, H., Myhre, G., Neubauer, D., van Noije, T., North, P., Olivié, D. J. L., Rémy,
706 S., Sogacheva, L., Takemura, T., Tsigaridis, K., and Tsyro, S. G.: AeroCom phase III
707 multi-model evaluation of the aerosol life cycle and optical properties using ground- and
708 space-based remote sensing as well as surface in situ observations, *Atmos. Chem. Phys.*,
709 21, 87-128, <https://doi.org/10.5194/acp-21-87-2021>, 2021.
- 710 Gu, Y. F., Zhang, W. S., Yang, Y. J., Wang, C., Streets, D. G., and Yim, S. H. L.: Assessing
711 outdoor air quality and public health impact attributable to residential black carbon
712 emissions in rural China, *Resour Conserv Recy*, 159, 104812,
713 <https://doi.org/10.1016/j.resconrec.2020.104812>, 2020.
- 714 Guan, D., Liu, Z., Geng, Y., Lindner, S., and Hubacek, K.: The gigatonne gap in China's
715 carbon dioxide inventories, *Nat. Clim. Change*, 2, 672-675,
716 <https://doi.org/10.1038/nclimate1560>, 2012.
- 717 Guerrette, J. J. and Henze, D. K.: Four-dimensional variational inversion of black carbon
718 emissions during ARCTAS-CARB with WRFDA-Chem, *Atmos. Chem. Phys.*, 17,
719 7605-7633, <https://doi.org/10.5194/acp-17-7605-2017>, 2017.
- 720 Han, Y. and Wang, Y.: Study on development, trend and countermeasures of coal industry in
721 Shanxi province, *China Economist*, 318, 22-25 (in Chinese), 2015.
- 722 Harmsen, M. J. H. M., van Dorst, P., van Vuuren, D. P., van den Berg, M., Van Dingenen, R.,
723 and Klimont, Z.: Co-benefits of black carbon mitigation for climate and air quality, *Clim.*
724 *Change*, 163, 1519-1538, <https://doi.org/10.1007/s10584-020-02800-8>, 2020.
- 725 Hu, Z. Y., Zhao, C., Huang, J. P., Leung, L. R., Qian, Y., Yu, H. B., Huang, L., and
726 Kalashnikova, O. V.: Trans-Pacific transport and evolution of aerosols: evaluation of
727 quasi-global WRF-Chem simulation with multiple observations, *Geosci. Model Dev.*, 9,
728 1725-1746, <https://doi.org/10.5194/gmd-9-1725-2016>, 2016.



- 729 Huang, L., Zhu, Y., Zhai, H., Xue, S., Zhu, T., Shao, Y., Liu, Z., Emery, C., Yarwood, G.,
730 Wang, Y., Fu, J., Zhang, K., and Li, L.: Recommendations on benchmarks for numerical
731 air quality model applications in China – Part 1: PM_{2.5} and chemical species, *Atmos.*
732 *Chem. Phys.*, 21, 2725-2743, <https://doi.org/10.5194/acp-21-2725-2021>, 2021.
- 733 Klimont, Z., Cofala, J., Xing, J., Wei, W., Zhang, C., Wang, S., Kejun, J., Bhandari, P.,
734 Mathur, R., Purohit, P., Rafaj, P., Chambers, A., Amann, M., and Hao, J.: Projections of
735 SO₂, NO_x and carbonaceous aerosols emissions in Asia, *Tellus B: Chem. Phys.*
736 *Meteorol.*, 61B, 602-617, <https://doi.org/10.1111/j.1600-0889.2009.00428.x>, 2009.
- 737 Kurokawa, J. and Ohara, T.: Long-term historical trends in air pollutant emissions in Asia:
738 Regional Emission inventory in ASia (REAS) version 3, *Atmos. Chem. Phys.*, 20,
739 12761-12793, <https://doi.org/10.5194/acp-20-12761-2020>, 2020.
- 740 Lei, Y., Zhang, Q., He, K. B., and Streets, D. G.: Primary anthropogenic aerosol emission
741 trends for China, 1990–2005, *Atmos. Chem. Phys.*, 11, 931-954,
742 <https://doi.org/10.5194/acp-11-931-2011>, 2011.
- 743 Li, M., Liu, H., Geng, G. N., Hong, C. P., Liu, F., Song, Y., Tong, D., Zheng, B., Cui, H. Y.,
744 Man, H. Y., Zhang, Q., and He, K. B.: Anthropogenic emission inventories in China: a
745 review, *Natl. Sci. Rev.*, 4, 834-866, <https://doi.org/10.1093/nsr/nwx150>, 2017.
- 746 Li, S. S., Yu, C., Chen, L. F., Tao, J. H., Letu, H., Ge, W., Si, Y. D., and Liu, Y.:
747 Inter-comparison of model-simulated and satellite-retrieved componential aerosol
748 optical depths in China, *Atmos. Environ.*, 141, 320-332,
749 <https://doi.org/10.1016/j.atmosenv.2016.06.075>, 2016a.
- 750 Li, Y., Henze, D. K., Jack, D., Henderson, B. H., and Kinney, P. L.: Assessing public health
751 burden associated with exposure to ambient black carbon in the United States, *Sci. Total*
752 *Environ.*, 539, 515-525, <https://doi.org/10.1016/j.scitotenv.2015.08.129>, 2016b.
- 753 Li, Z., Tan, H., Zheng, J., Liu, L., Qin, Y., Wang, N., Li, F., Li, Y., Cai, M., Ma, Y., and
754 Chan, C. K.: Light absorption properties and potential sources of particulate brown
755 carbon in the Pearl River Delta region of China, *Atmos. Chem. Phys.*, 19, 11669-11685,
756 <https://doi.org/10.5194/acp-19-11669-2019>, 2019.



- 757 Li, Z. Q., Xu, H., Li, K. T., Li, D. H., Xie, Y. S., Li, L., Zhang, Y., Gu, X. F., Zhao, W., Tian,
758 Q. J., Deng, R. R., Su, X. L., Huang, B., Qiao, Y. L., Cui, W. Y., Hu, Y., Gong, C. L.,
759 Wang, Y. Q., Wang, X. F., Wang, J. P., Du, W. B., Pan, Z. Q., Li, Z. Z., and Bu, D.:
760 Comprehensive Study of Optical, Physical, Chemical, and Radiative Properties of Total
761 Columnar Atmospheric Aerosols over China: An Overview of Sun–Sky Radiometer
762 Observation Network (SONET) Measurements, *Bull. Am. Meteorol. Soc.*, 99, 739-755,
763 <https://doi.org/10.1175/BAMS-D-17-0133.1>, 2018.
- 764 Liang, F. C., Xiao, Q. Y., Huang, K. Y., Yang, X. L., Liu, F. C., Li, J. X., Lu, X. F., Liu, Y.,
765 and Gu, D. F.: The 17-y spatiotemporal trend of PM_{2.5} and its mortality burden in
766 China, *Proc. Natl. Acad. Sci. U.S.A.*, 117, 25601-25608,
767 <https://doi.org/10.1073/pnas.1919641117>, 2020.
- 768 Liu, Y., Wang, M., Qian, Y., and Ding, A.: A Strong Anthropogenic Black Carbon Forcing
769 Constrained by Pollution Trends Over China, *Geophys. Res. Lett.*, 49, e2022GL098965,
770 <https://doi.org/10.1029/2022gl098965>, 2022.
- 771 Louis, C., Liu, Y., Tassel, P., Perret, P., Chaumond, A., and André, M.: PAH, BTEX,
772 carbonyl compound, black-carbon, NO₂ and ultrafine particle dynamometer bench
773 emissions for Euro 4 and Euro 5 diesel and gasoline passenger cars, *Atmos. Environ.*,
774 141, 80-95, <https://doi.org/10.1016/j.atmosenv.2016.06.055>, 2016.
- 775 Lu, Y., Wang, Q. G., Zhang, X. H., Qian, Y., and Qian, X.: China's black carbon emission
776 from fossil fuel consumption in 2015, 2020, and 2030, *Atmos. Environ.*, 212, 201-207,
777 <https://doi.org/10.1016/j.atmosenv.2019.04.032>, 2019.
- 778 Lu, Z., Zhang, Q., and Streets, D. G.: Sulfur dioxide and primary carbonaceous aerosol
779 emissions in China and India, 1996–2010, *Atmos. Chem. Phys.*, 11, 9839-9864,
780 <https://doi.org/10.5194/acp-11-9839-2011>, 2011.
- 781 McDuffie, E. E., Smith, S. J., O'Rourke, P., Tibrewal, K., Venkataraman, C., Marais, E. A.,
782 Zheng, B., Crippa, M., Brauer, M., and Martin, R. V.: A global anthropogenic emission
783 inventory of atmospheric pollutants from sector- and fuel-specific sources (1970–2017):



- 784 an application of the Community Emissions Data System (CEDS), *Earth Syst. Sci. Data*,
785 12, 3413-3442, <https://doi.org/10.5194/essd-12-3413-2020>, 2020.
- 786 Middleton, N.: Variability and Trends in Dust Storm Frequency on Decadal Timescales:
787 Climatic Drivers and Human Impacts, *Geosciences*, 9,
788 <https://doi.org/10.3390/geosciences9060261>, 2019.
- 789 Qin, Y. and Xie, S. D.: Spatial and temporal variation of anthropogenic black carbon
790 emissions in China for the period 1980–2009, *Atmos. Chem. Phys.*, 12, 4825-4841,
791 <https://doi.org/10.5194/acp-12-4825-2012>, 2012.
- 792 Qin, Y., Fang, Y. Y., Li, X. Y., Naik, V., Horowitz, L. W., Liu, J. F., Scovronick, N., and
793 Mauzerall, D. L.: Source attribution of black carbon affecting regional air quality,
794 premature mortality and glacial deposition in 2000, *Atmos. Environ.*, 206, 144-155,
795 <https://doi.org/10.1016/j.atmosenv.2019.02.048>, 2019.
- 796 Saikawa, E., Naik, V., Horowitz, L. W., Liu, J., and Mauzerall, D. L.: Present and potential
797 future contributions of sulfate, black and organic carbon aerosols from China to global
798 air quality, premature mortality and radiative forcing, *Atmos. Environ.*, 43, 2814-2822,
799 <https://doi.org/10.1016/j.atmosenv.2009.02.017>, 2009.
- 800 Samset, B. H., Fuglestedt, J. S., and Lund, M. T.: Delayed emergence of a global
801 temperature response after emission mitigation, *Nat. Commun.*, 11, 3261,
802 <https://doi.org/10.1038/s41467-020-17001-1>, 2020.
- 803 Schroeder, W., Prins, E., Giglio, L., Csiszar, I., Schmidt, C., Morisette, J., and Morton, D.:
804 Validation of GOES and MODIS active fire detection products using ASTER and
805 ETM+ data, *Remote Sens. Environ.*, 112, 2711-2726,
806 <https://doi.org/10.1016/j.rse.2008.01.005>, 2008.
- 807 Schutgens, N., Dubovik, O., Hasekamp, O., Torres, O., Jethva, H., Leonard, P. J. T., Litvinov,
808 P., Redemann, J., Shinozuka, Y., de Leeuw, G., Kinne, S., Popp, T., Schulz, M., and
809 Stier, P.: AEROCOM and AEROSAT AAOD and SSA study - Part 1: Evaluation and
810 intercomparison of satellite measurements, *Atmos. Chem. Phys.*, 21, 6895-6917,
811 <https://doi.org/10.5194/acp-21-6895-2021>, 2021.



- 812 Shindell, D., Kuylensstierna, J. C. I., Vignati, E., van Dingenen, R., Amann, M., Klimont, Z.,
813 Anenberg, S. C., Muller, N., Janssens-Maenhout, G., Raes, F., Schwartz, J., Faluvegi, G.,
814 Pozzoli, L., Kupiainen, K., Höglund-Isaksson, L., Emberson, L., Streets, D.,
815 Ramanathan, V., Hicks, K., Oanh, N. T. K., Milly, G., Williams, M., Demkine, V., and
816 Fowler, D.: Simultaneously Mitigating Near-Term Climate Change and Improving
817 Human Health and Food Security, *Science*, 335, 183-189,
818 <https://doi.org/doi:10.1126/science.1210026>, 2012.
- 819 Streets, D. G., Yarber, K. F., Woo, J. H., and Carmichael, G. R.: Biomass burning in Asia:
820 Annual and seasonal estimates and atmospheric emissions, *Global Biogeochem. Cycles*,
821 17, 1-20, <https://doi.org/10.1029/2003gb002040>, 2003.
- 822 Tao, J., Zhang, L., Cao, J., and Zhang, R.: A review of current knowledge concerning PM_{2.5}
823 chemical composition, aerosol optical properties and their relationships across China,
824 *Atmos. Chem. Phys.*, 17, 9485-9518, <https://doi.org/10.5194/acp-17-9485-2017>, 2017.
- 825 The Central People's Government of the People's Republic of China. Shanxi Province
826 eliminated more than 200 million tons of backward coal production capacity from 2008
827 to 2010. Accessed: [20 January 2023].
828 http://www.gov.cn/jrzq/2011-05/12/content_1862911.htm., 2011.
- 829 Tsinghua University: The Multi-resolution Emission Inventory for China (MEIC) [dataset],
830 Accessed: [25 May 2022]. <http://meicmodel.org.cn>. 2023.
- 831 Vignati, E., Karl, M., Krol, M., Wilson, J., Stier, P., and Cavalli, F.: Sources of uncertainties
832 in modelling black carbon at the global scale, *Atmos. Chem. Phys.*, 10, 2595-2611,
833 <https://doi.org/10.5194/acp-10-2595-2010>, 2010.
- 834 Wang, P., Wang, H., Wang, Y. Q., Zhang, X. Y., Gong, S. L., Xue, M., Zhou, C. H., Liu, H.
835 L., An, X. Q., Niu, T., and Cheng, Y. L.: Inverse modeling of black carbon emissions
836 over China using ensemble data assimilation, *Atmos. Chem. Phys.*, 16, 989-1002,
837 <https://doi.org/10.5194/acp-16-989-2016>, 2016.
- 838 Wang, R.: *Global Emission Inventory and Atmospheric Transport of Black Carbon:
839 Evaluation of the Associated Exposure.*, Springer, Berlin Heidelberg, 2015.



- 840 Wang, R., Andrews, E., Balkanski, Y., Boucher, O., Myhre, G., Samset, B. H., Schulz, M.,
841 Schuster, G. L., Valari, M., and Tao, S.: Spatial Representativeness Error in the
842 Ground-Level Observation Networks for Black Carbon Radiation Absorption, *Geophys.*
843 *Res. Lett.*, 45, 2106-2114, <https://doi.org/10.1002/2017GL076817>, 2018.
- 844 Wang, R., Tao, S., Balkanski, Y., Ciais, P., Boucher, O., Liu, J., Piao, S., Shen, H., Vuolo, M.
845 R., Valari, M., Chen, H., Chen, Y., Cozic, A., Huang, Y., Li, B., Li, W., Shen, G., Wang,
846 B., and Zhang, Y.: Exposure to ambient black carbon derived from a unique inventory
847 and high-resolution model, *Proc. Natl. Acad. Sci. U.S.A.*, 111, 2459-2463,
848 <https://doi.org/10.1073/pnas.1318763111>, 2014.
- 849 Wang, R., Tao, S., Wang, W., Liu, J., Shen, H., Shen, G., Wang, B., Liu, X., Li, W., Huang,
850 Y., Zhang, Y., Lu, Y., Chen, H., Chen, Y., Wang, C., Zhu, D., Wang, X., Li, B., Liu, W.,
851 and Ma, J.: Black carbon emissions in China from 1949 to 2050, *Environ. Sci. Technol.*,
852 46, 7595-7603, <https://doi.org/10.1021/es3003684>, 2012.
- 853 Wang, X., Wang, Y. X., Hao, J. M., Kondo, Y., Irwin, M., Munger, J. W., and Zhao, Y. J.:
854 Top-down estimate of China's black carbon emissions using surface observations:
855 Sensitivity to observation representativeness and transport model error, *J. Geophys.*
856 *Res.-Atmos.*, 118, 5781-5795, <https://doi.org/10.1002/jgrd.50397>, 2013.
- 857 Wang, Y., Li, X., Shi, Z., Huang, L., Li, J., Zhang, H., Ying, Q., Wang, M., Ding, D., Zhang,
858 X., and Hu, J.: Premature Mortality Associated with Exposure to Outdoor Black Carbon
859 and Its Source Contributions in China, *Resour. Conserv. Recycl.*, 170, 105620,
860 <https://doi.org/10.1016/j.resconrec.2021.105620>, 2021.
- 861 WorldPop (www.worldpop.org - School of Geography and Environmental Science,
862 University of Southampton; Department of Geography and Geosciences, University of
863 Louisville; Departement de Geographie, Universite de Namur) and Center for
864 International Earth Science Information Network (CIESIN), Columbia University.
865 Accessed: [20 October 2022]. <https://dx.doi.org/10.5258/SOTON/WP00674>, 2018.



- 866 Xiao, Q. Y., Chang, H. H., Geng, G. N., and Liu, Y.: An Ensemble Machine-Learning Model
867 To Predict Historical PM_{2.5} Concentrations in China from Satellite Data, *Environ. Sci.*
868 *Technol.*, 52, 13260-13269, <https://doi.org/10.1021/acs.est.8b02917>, 2018.
- 869 Xin, J., Wang, Y., Pan, Y., Ji, D., Liu, Z., Wen, T., Wang, Y., Li, X., Sun, Y., Sun, J., Wang,
870 P., Wang, G., Wang, X., Cong, Z., Song, T., Hu, B., Wang, L., Tang, G., Gao, W., Guo,
871 Y., Miao, H., Tian, S., and Wang, L.: The Campaign on Atmospheric Aerosol Research
872 Network of China: CARE-China, *Bull. Am. Meteorol. Soc.*, 96, 1137-1155,
873 <https://doi.org/10.1175/BAMS-D-14-00039.1>, 2015.
- 874 Xue, T., Zheng, Y., Li, X., Liu, J., Zhang, Q., and Zhu, T.: A component-specific
875 exposure-mortality model for ambient PM_{2.5} in China: findings from nationwide
876 epidemiology based on outputs from a chemical transport model, *Faraday Discuss.*, 226,
877 551-568, <https://doi.org/10.1039/d0fd00093k>, 2021.
- 878 Yang, J., Zhao, T. L., Cheng, X. G., Ren, Z. H., Meng, L., He, Q., Tan, C. H., Zhu, Y., Zhu,
879 C. Z., and Wu, Z. Y.: Temporal and spatial variations of sandstorm and the related
880 meteorological influences over northern China from 2000 to 2019, *Acta Sci. Circum.*, 41,
881 2966-2975 (in Chinese), <https://doi.org/10.13671/j.hjkxxb.2021.0234>, 2021.
- 882 Yang, Y. and Zhao, Y.: Quantification and evaluation of atmospheric pollutant emissions
883 from open biomass burning with multiple methods: a case study for the Yangtze River
884 Delta region, China, *Atmos. Chem. Phys.*, 19, 327-348,
885 <https://doi.org/10.5194/acp-19-327-2019>, 2019.
- 886 Zhang, L., Henze, D. K., Grell, G. A., Carmichael, G. R., Boussez, N., Zhang, Q., Torres,
887 O., Ahn, C., Lu, Z., Cao, J., and Mao, Y.: Constraining black carbon aerosol over Asia
888 using OMI aerosol absorption optical depth and the adjoint of GEOS-Chem, *Atmos.*
889 *Chem. Phys.*, 15, 10281-10308, <https://doi.org/10.5194/acp-15-10281-2015>, 2015.
- 890 Zhang, L., Henze, D. K., Grell, G. A., Torres, O., Jethva, H., and Lamsal, L. N.: What factors
891 control the trend of increasing AAOD over the United States in the last decade?, *J.*
892 *Geophys. Res.-Atmos.*, 122, 1797-1810, <https://doi.org/10.1002/2016jd025472>, 2017.



- 893 Zhang, Q., Zheng, Y., Tong, D., Shao, M., Wang, S., Zhang, Y., Xu, X., Wang, J., He, H.,
894 Liu, W., Ding, Y., Lei, Y., Li, J., Wang, Z., Zhang, X., Wang, Y., Cheng, J., Liu, Y., Shi,
895 Q., Yan, L., Geng, G., Hong, C., Li, M., Liu, F., Zheng, B., Cao, J., Ding, A., Gao, J., Fu,
896 Q., Huo, J., Liu, B., Liu, Z., Yang, F., He, K., and Hao, J.: Drivers of improved PM_{2.5}
897 air quality in China from 2013 to 2017, *Proc. Natl. Acad. Sci. U.S.A.*, 116, 24463-24469,
898 <https://doi.org/10.1073/pnas.1907956116>, 2019.
- 899 Zhao, X. F., Zhao, Y., Chen, D., Li, C. Y., and Zhang, J.: Top-down estimate of black carbon
900 emissions for city clusters using ground observations: a case study in southern Jiangsu,
901 China, *Atmos. Chem. Phys.*, 19, 2095-2113, <https://doi.org/10.5194/acp-19-2095-2019>,
902 2019.
- 903 Zheng, B., Geng, G., Ciais, P., Davis Steven, J., Martin Randall, V., Meng, J., Wu, N.,
904 Chevallier, F., Broquet, G., Boersma, F., van der, A. R., Lin, J., Guan, D., Lei, Y., He,
905 K., and Zhang, Q.: Satellite-based estimates of decline and rebound in China's CO₂
906 emissions during COVID-19 pandemic, *Sci. Adv.*, 6, eabd4998,
907 <https://doi.org/10.1126/sciadv.abd4998>, 2020.
- 908 Zhi, G., Zhang, Y., Sun, J., Cheng, M., Dang, H., Liu, S., Yang, J., Zhang, Y., Xue, Z., Li, S.,
909 and Meng, F.: Village energy survey reveals missing rural raw coal in northern China:
910 Significance in science and policy, *Environ. Pollut.*, 223, 705-712,
911 <https://doi.org/10.1016/j.envpol.2017.02.009>, 2017.
- 912 Zhu, C. S., Qu, Y., Huang, H., Chen, J., Dai, W. T., Huang, R. J., and Cao, J. J.: Black
913 Carbon and Secondary Brown Carbon, the Dominant Light Absorption and Direct
914 Radiative Forcing Contributors of the Atmospheric Aerosols Over the Tibetan Plateau,
915 *Geophys. Res. Lett.*, 48, 1-9, <https://doi.org/10.1029/2021gl092524>, 2021.
- 916 Zhu, X., Yun, X., Meng, W., Xu, H., Du, W., Shen, G., Cheng, H., Ma, J., and Tao, S.:
917 Stacked Use and Transition Trends of Rural Household Energy in Mainland China,
918 *Environ. Sci. Technol.*, 53, 521-529, <https://doi.org/10.1021/acs.est.8b04280>, 2019.
- 919
920



921 **Figure captions**

922 Figure 1 The top-down inversion approach to estimate monthly BC emissions.

923 Figure 2 Comparison between XGBoost prediction and OMI observation AAOD for
924 2005-2020.

925 Figure 3 (a) Spatial distribution of multiyear average AAOD during 2000-2020 and (b-h)
926 interannual variations of AAOD for China and six key regions in 2000-2020. The grey and
927 white present Phase 1 (2000-2012) and Phase 2 (2013-2020), respectively. The red dots and
928 dashed line represent time series of monthly AAOD (left vertical axis). The black solid lines
929 represent the interannual variability after removing the seasonal change through time-series
930 decomposition (right vertical axis). The straight red, blue and yellow lines present the linear
931 trends of AAOD for different phases (right vertical axis). The annual variation rates (1/yr)
932 during different phases with significance levels (* $p < 0.05$, ** $p < 0.01$, *** $p < 0.001$) are
933 presented.

934 Figure 4 Correlation between simulated and observed monthly surface BC concentrations in
935 China. Simulations were conducted based on prior and posterior BC emissions, while
936 observations were collected from publications.

937 Figure 5 Comparisons between posterior and various “bottom-up” BC emission estimates in
938 China during 2000-2020. (a) Multiyear average spatial distribution of prior BC emissions
939 (MEIC+GFED), (b) posterior BC emissions, and (c) their relative differences. (d) Long-term
940 variability in the relative differences between posterior and various “bottom-up” BC emission
941 estimates, with five-year intervals. (e) Long-term variability in normalized posterior and
942 various “bottom-up” BC emission estimates (relative to 2000). The grey area indicates the
943 period with declining national BC emissions. (f) Long-term variability in the relative



944 differences between prior (MEIC+GFED) and posterior BC emissions by region and land use
945 type.

946 Figure 6 The annual (a) prior BC emissions, (b) posterior BC emissions (three times of total
947 emissions of January, April, July and October) and (c) their relative differences during
948 2000-2020 (with a five-year interval).

949 Figure 7 Changes in provincial BC emission intensity (annual BC emissions per km²) in
950 posterior BC estimates. (a,b) Spatial distribution of the interannual change rate of BC
951 emission intensity by province during 2000-2010 and 2010-2020. (c,d) Relationships between
952 interannual BC emission change rate and rural population fraction, proportion of coal
953 production, and industrial GDP for each province. The x and y-axes present the rural
954 population fraction of each province and provincial proportion of coal production to the
955 national total for the middle year of the concerned period (i.e., 2005 for c and 2015 for d),
956 respectively. Circle size represents provincial industrial GDP level. Statistics of population,
957 coal production, and GDP were obtained from the National Bureau of Statistics
958 (<https://data.stats.gov.cn/>; last accessed on 15 February 2023).

959 Figure 8 Relative changes of the prior and posterior BC, OC, PM_{2.5} emissions (left vertical
960 axis) and the posterior BC and PM_{2.5} concentrations (right vertical axis) during 2000-2020
961 compared with those of 2000 (with a five-year interval). OC and PM_{2.5} emissions are
962 obtained from the Multi-resolution Emission Inventory for China (MEIC,
963 <http://www.meicmodel.org/>; last access: 25 May 2022). PM_{2.5} concentrations are obtained
964 from Tracking Air Pollution in China (TAP, <http://tapdata.org.cn/>; last access: 31 January
965 2023).

966 Figure 9 Drivers of changing premature mortality associated with BC exposure in China
967 during 2000-2020. Error bars show the 95% CI of estimates in this study.



968 Figure 10 (a) Long-term variability of the normalized prior and posterior BC emissions in
969 China during 2000-2020 (compared with 2000, solid lines with left vertical axis, with a
970 five-year interval), and relative difference between the posterior and prior emissions (dashed
971 lines with right vertical axis) for the base case, Test 1, Test 2, Test 3 and Test 4. (b) Relative
972 difference in the Eastern China and the rest of China for the base case (red lines and marks),
973 Test 1 (green lines and marks), Test 2 (purple lines and marks), Test 3 (blue lines and marks)
974 and Test 4 (yellow lines and marks).

975

976



977 **Tables**

978 **Table 1 The multiyear average relative differences between the posterior and various**
979 **“bottom-up” estimates of BC emissions by region.**

Region	CEDS	PKU	EDGAR	REAS	MEIC	Average
BTH	1.20	0.31	2.37	0.69	0.99	1.11
FWP	0.82	1.44	1.26	1.53	1.56	2.12
YRD	0.78	1.15	2.10	2.15	2.65	1.32
PRD	3.25	2.23	6.47	3.03	3.17	1.77
SCB	2.20	0.56	3.66	1.51	2.70	3.63
NE	5.36	4.66	7.10	5.89	6.81	5.97
Other	3.42	1.98	5.10	3.76	3.62	3.57
China	2.75	1.72	4.27	2.90	3.26	2.98

980

981



982 **Table 2 The annual posterior BC emission intensity of different land-use types in**
983 **2000-2020 (with a five-year interval).** The annual emission intensity was estimated as three
984 times sum of BC emission intensity of January, April, July and October. “Urban” includes
985 city and building categories, and “Rural” includes cropland and countryside categories (Unit:
986 Mg/km²/yr).

	2000	2005	2010	2015	2020	Average
City	2.26	2.19	2.32	1.98	1.68	2.09
Building	1.57	1.70	1.68	1.42	1.23	1.52
Countryside	1.59	1.74	1.77	1.66	1.43	1.64
Cropland	1.46	1.61	1.60	1.37	1.22	1.45
Forest	0.89	0.93	0.97	0.71	0.70	0.84
Grassland	0.35	0.39	0.35	0.27	0.27	0.33
Unused	0.11	0.13	0.12	0.11	0.09	0.11
Urban	1.98	1.99	2.07	1.75	1.50	1.86
Rural	1.47	1.62	1.62	1.39	1.24	1.47

987

988



989 **Table 3 The annual all-cause premature mortality associated with BC exposure by**
 990 **province in mainland China during 2000-2020 with a five-year interval (Unit:**
 991 **cases/grid). Locations of provinces are shown in Figure S1a.**

	2000	2005	2010	2015	2020	Average
Shanghai	765	917	1211	1485	1023	1080
Beijing	299	500	569	678	843	578
Tianjin	322	438	554	661	797	555
Jiangsu	249	351	419	488	390	379
Henan	282	353	307	295	404	328
Shandong	218	315	332	360	386	322
Anhui	159	233	246	249	235	224
Liaoning	252	206	197	171	164	198
Hebei	142	182	173	182	221	180
Chongqing	184	208	182	149	174	179
Hubei	126	182	179	140	153	156
Jilin	151	145	150	155	137	148
Zhejiang	102	131	153	171	163	144
Hunan	119	165	150	125	158	143
Guangdong	109	129	155	121	140	131
Shanxi	140	155	97	94	158	129
Sichuan	90	108	95	76	82	90
Guizhou	80	93	81	87	96	88
Jiangxi	66	93	94	79	99	86
Shannxi	70	88	69	58	84	74
Heilongjiang	64	64	75	83	79	73
Fujian	59	63	72	58	61	63
Guangxi	51	70	72	53	59	61
Hainan	34	43	46	32	43	40
Yunnan	31	38	36	37	43	37
Ningxia	25	36	24	25	35	29
Gansu	17	22	14	12	16	16
Inner Mongolia	5	6	5	4	5	5
Qinghai	2	2	1	1	2	2
Xinjiang	1	1	1	1	1	1
Tibet	0	0	0	0	0	0

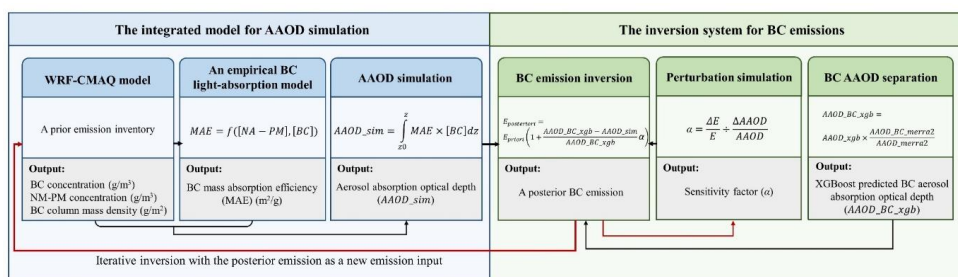
992

993



994 **Figures**

995 **Figure 1**



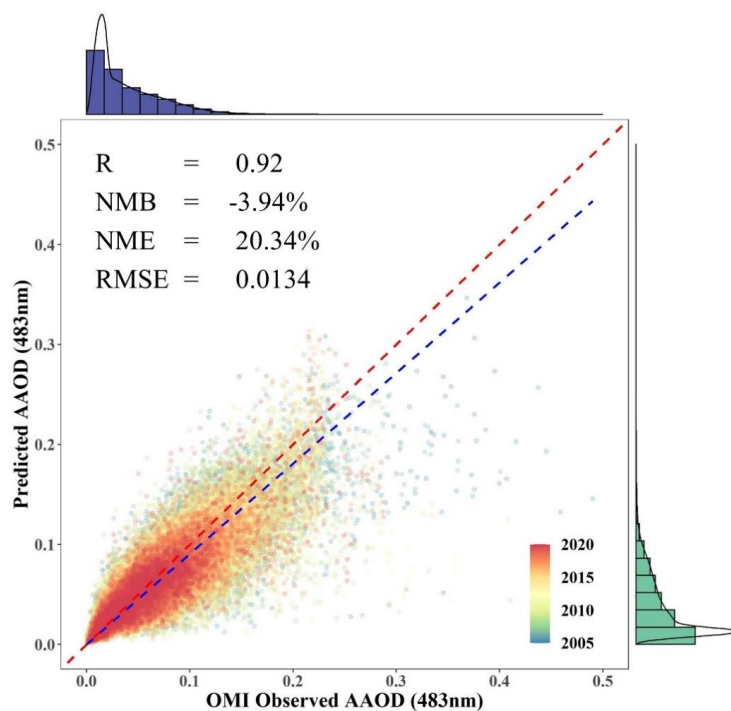
996

997

998



999 **Figure 2**



1000

1001 Note: The NMB, NME and RMSE were calculated using following equations (P and O indicate the results
1002 from XGBoost prediction and OMI observation, respectively):

1003
$$NMB = \frac{\sum_{i=1}^n (P_i - O_i)}{\sum_{i=1}^n O_i} \times 100\%$$

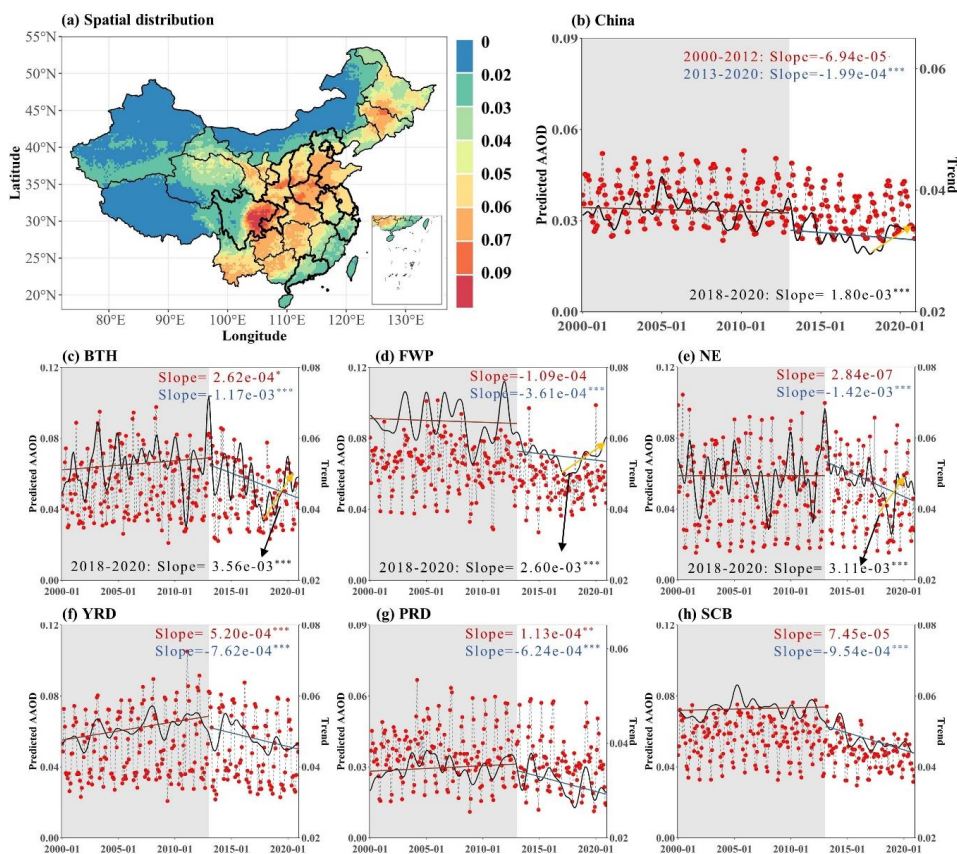
1004
$$NME = \frac{\sum_{i=1}^n |P_i - O_i|}{\sum_{i=1}^n O_i}$$

1005
$$RMSE = \sqrt{\frac{1}{n} \sum_{i=1}^n (P_i - O_i)^2}$$

1006



1007 **Figure 3**



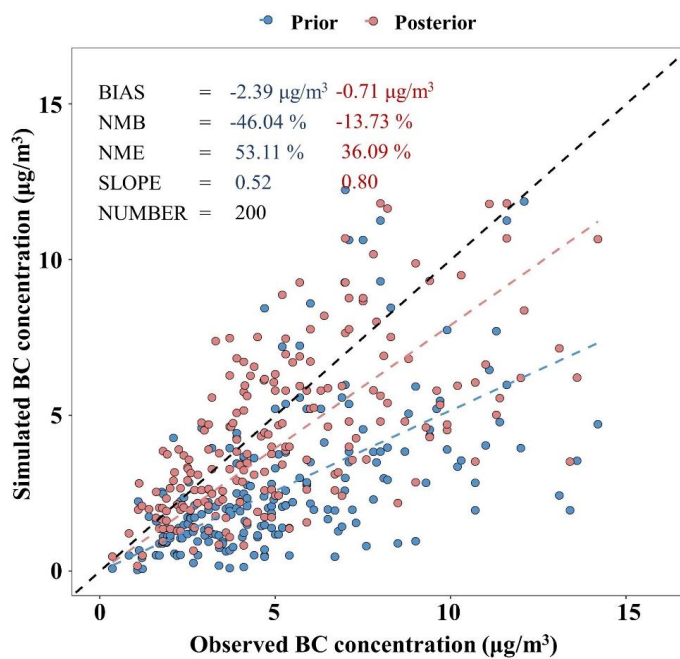
1008

1009

1010



1011 **Figure 4**



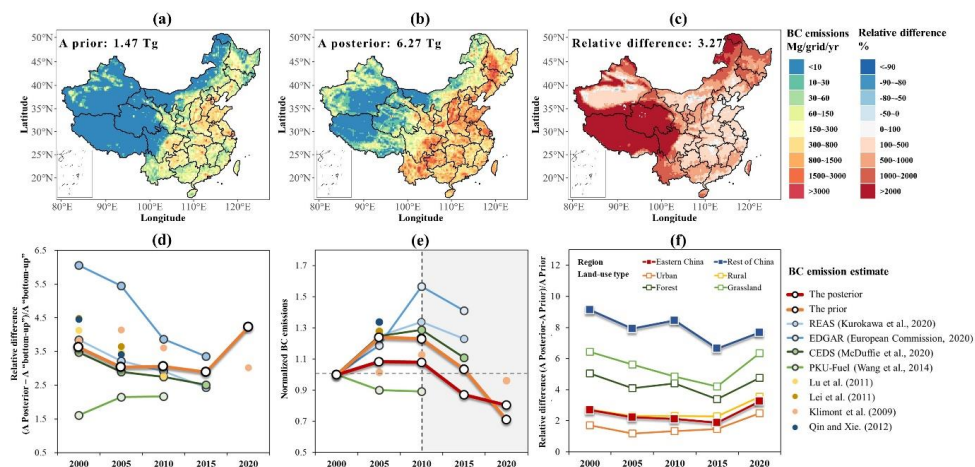
1012

1013

1014



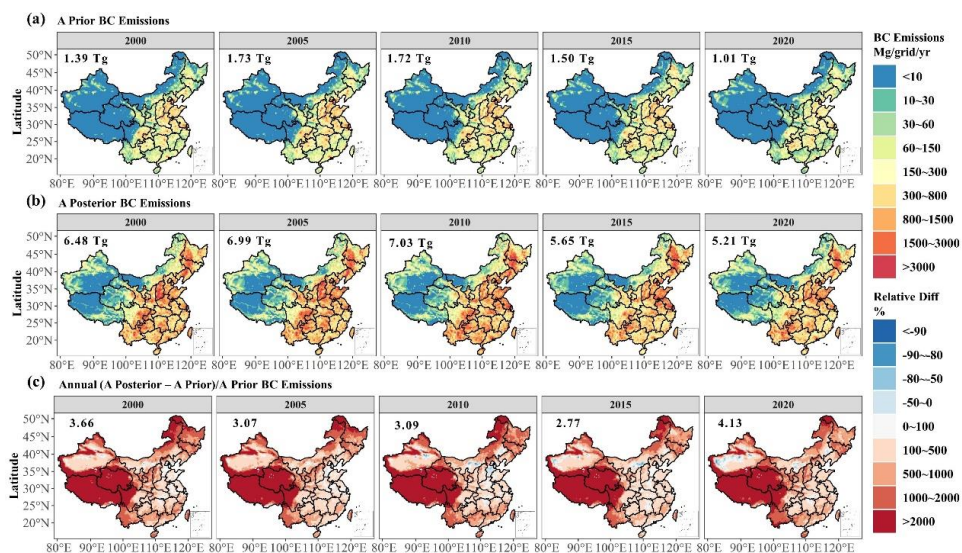
1015 **Figure 5**



1016
 1017



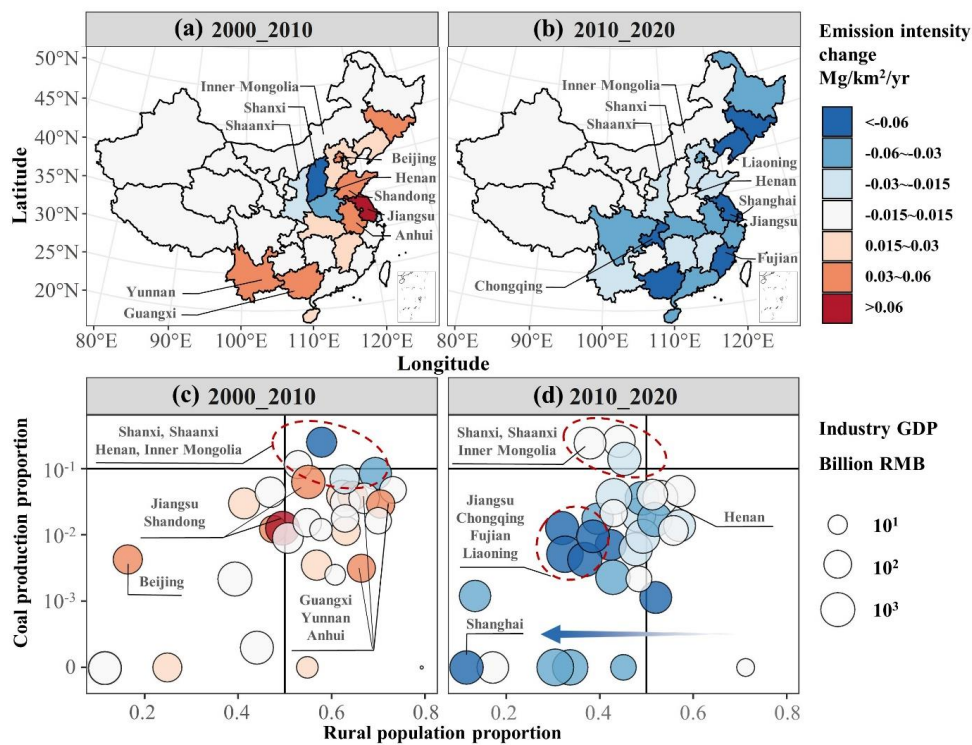
1018 **Figure 6**



1019
 1020



1021 **Figure 7**



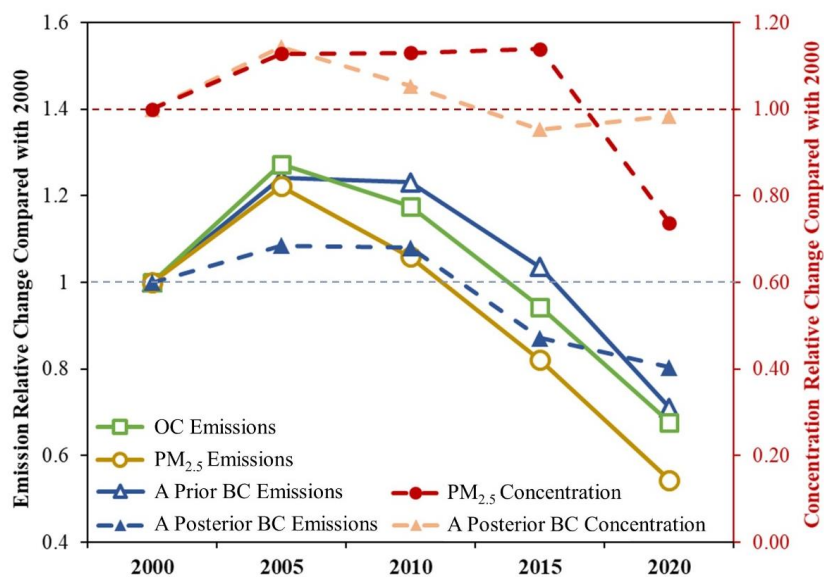
1022

1023



1024 **Figure 8**

1025



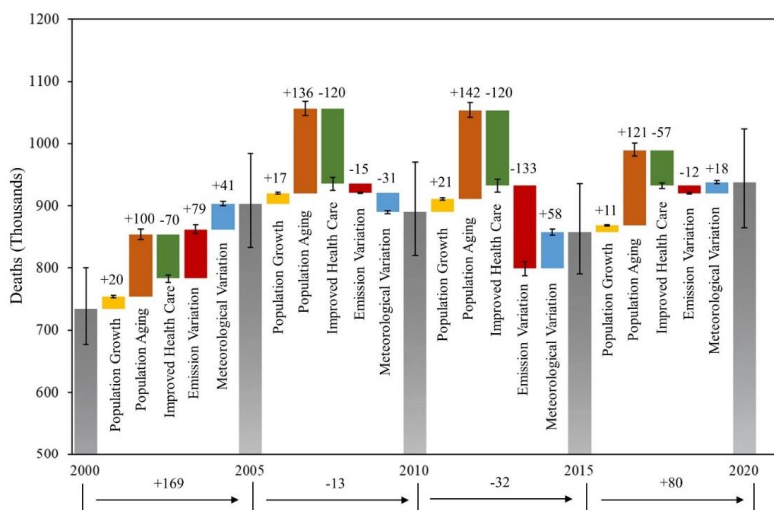
1026

1027

1028



1029 **Figure 9**



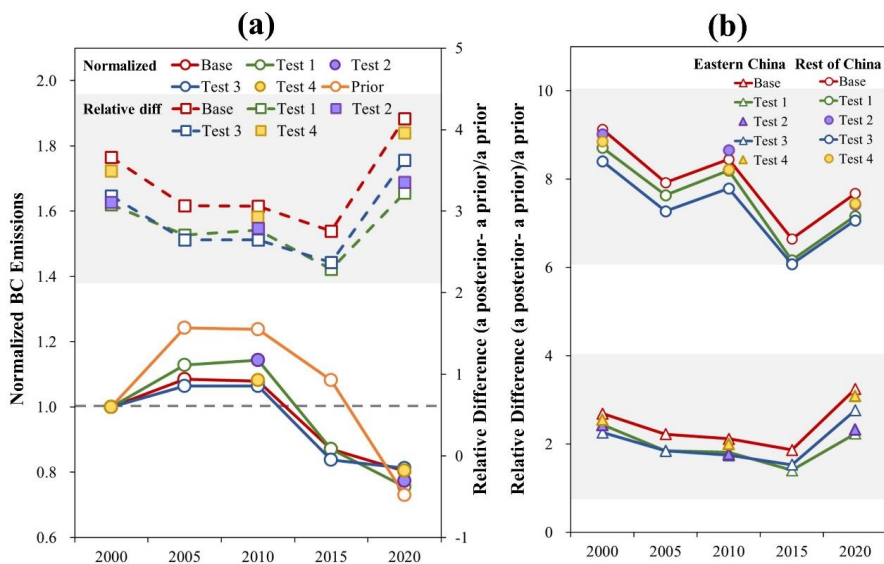
1030

1031



1032 **Figure 10**

1033



1034

1035

1036